Materials Science

Research article

Synthesis, characterization, thermal and mechanical behavior of polypropylene hybrid composites embedded with CaCO₃ and graphene nano-platelets (GNPs) for structural applications

R. Daulath Banu[1], R. Karunanithi[2,*], S. Sivasankaran[3], B. Subramanian[4] and Abdullah A. Alhomidan[5]

[1] Department of Polymer Engineering, B. S. Abdur Rahman Crescent Institute of Science and Technology, Chennai, 600048, India

[2] Department of Mechanical Engineering, B. S. Abdur Rahman Crescent Institute of Science and Technology, Chennai, 600048, India

[3] Department of Mechanical Engineering, College of Engineering, Qassim University, Buraydah 51452, Saudi Arabia

[4] Electroplating and Metal Finishing division, CSIR, Central Electro Chemical Research Institute, Karaikudi 600 003, Tamilnadu, India

[5] Department of Mechanical Engineering, College of Engineering, University of Akron, Ohio 44325-3903, United States

* Correspondence: Email: karunaponni@gmail.com; karunanithi@crescent.education.

Abstract: In this study, ultra-fine graphene nanoplatelets (GNPs) were employed as nanofillers to reinforce a polypropylene (PP) matrix. This was done in conjunction with a polypropylene grafted maleic anhydride (PP-MAH) compatibilizer and calcium carbonate (CaCO₃), with the aim of improving the mechanical and thermal properties of the resulting hybrid composites. Formulations for the hybrid composites were fabricated by compounding the PP matrix with varying weight percentages of GNPs (x = 0.5, 1.0, 1.5, 2.0), 2 wt.% CaCO₃, and 5 wt.% PP-MAH using a twin-screw extruder followed by injection molding. This research thoroughly investigates the mechanical and thermal characteristics. X-ray diffraction (XRD), X-ray photoelectron spectroscopy (XPS), and Fourier-transform infrared spectroscopy (FTIR) results confirm the successful development of hybrid composites. The thermal stability, crystallization temperature, melting temperature, tensile strength, flexural strength, and impact resistance were evaluated using differential scanning calorimetry (DSC), thermogravimetric

analysis (TGA), universal testing machine, and low-velocity impact tester, respectively. The results indicated a significant improvement in the tensile strength of the PP matrix with the addition of GNPs, with the highest enhancement observed at 1.5 wt.% GNP loading, where the tensile strength reached a maximum of 40.54 MPa. This improvement was attributed to the proper interconnection, bonding, and compounding of PP with GNPs, thus leading to an increase in the load transfer efficiency.

Abbreviations: PP: Polypropylene; TGA: Thermogravimetric analysis; PP-MAH: Maleic anhydride grafted PP; DSC: Differential scanning calorimetry; PET: Polyethylene terephthalate; XRD: X-ray diffraction; GNPs: Graphene nano-platelets; XPS: X-ray photoelectron spectroscopy; CNTs: Carbon nanotubes; FEG-HRSEM: Field emission gun high-resolution SEM; HDPE: High-density polyethylene; EDS: Energy-dispersive X-ray spectroscopy; FTIR: Fourier-transform infrared spectroscopy; SEM: Scanning electron microscopy

1. Introduction

Polypropylene (PP) has seen a significant surge in applications, from automotive to various industrial sectors, thanks to its remarkable mechanical strength and favorable thermal and electrical properties. Despite its advantages, such as abundant raw materials, non-toxicity, ease of processing, and cost-effectiveness [1], PP encounters strength challenges in diverse contexts. Research initiatives aim to enhance the performance and thermal characteristics of neat polymer blends, often involving the incorporation of nano-fillers [2–4]. Common fillers such as talc, calcium carbonate ($CaCO_3$), mica, wollastonite, and kaolin have become standard in the plastics industry, aiming to reduce production costs of molded components. These fillers play a pivotal role in improving the working properties, including flexural strength, rigidity, durability, and hardness [5]. Typically, these composite structures are systematically dispersed, with an effective polymeric matrix where small filler and/or fiber particles. Drawing insights from prior studies on thermoplastic polymers incorporated with graphene nano-particles (GNPs) [6–13], it is evident that the performance of GNP-based composites depends on multiple factors. These factors encompass the aspect ratio of the filler, the dispersion and orientation of GNPs within the matrix, the interfacial interaction between GNPs and the matrix, the selected processing method, and the choice of matrix.

Despite the thermodynamic immiscibility of many polymers, polymer blending offers a cost-effective means to create materials with desired properties [14]. However, this immiscibility can lead to poor interfacial adhesion, resulting in inferior properties. Stabilizing morphology through compatibilizers is crucial to achieve an enhanced performance [15]. It is essential to achieve a stabilized morphology and enhanced properties, compatibilization, either non-reactive or reactive. Non-reactive methods involve adding small amounts of third components to blends, such as block or graft co-polymers, thus promoting interactions with each polymer component. Reactive compatibilization involves in-situ copolymer formation during processing [16]. Another effective strategy involves nanofillers for compatibilization in immiscible blends [17]. Notably, the non-reactive method of maleic anhydride grafted polypropylene (PP-MAH) improves interfacial adhesion within the matrix.

Compatibilized composites display a higher yield strength, thus establishing a converse relationship compared to unmodified composites [18]. Recently, graphene has gained significant attention, especially with the addition of GNPs, as it was proven to improve the mechanical and thermal properties. Wang et al. [19] demonstrated a synergistic effect of GNPs and carbon nanotubes (CNTs) when incorporated into high-density polyethylene (HDPE), which results in improved electrical properties, though with a slight reduction in the mechanical properties. To reinforce the mechanical and thermal performance of PP products, this study explores the use of surface-modified kaolin in PP-MAH/M-kaolin composites. Characterization involves Fourier-transform infrared spectroscopy (FTIR) [20], scanning electron microscopy (SEM), and thermogravimetric analysis (TGA) [21].

Meena et al. [22] conducted a comprehensive study to explore the impact of fly ash on the thermo-mechanical and mechanical behavior of injection-molded PP matrix composites. Concerning the thermo-mechanical behavior, the addition of fly ash significantly reduced the coefficient of thermal expansion (CTE) in the composites. Quantitatively, the CTE decreased from 10.82 to 7.15 μm/m·°C with an increasing fly ash content, thus indicating a clear influence on the dimensional stability of the composites. Additionally, fly ash inclusion substantially enhanced the flexural modulus from 3200 MPa for pure PP to 4500 MPa, highlighting a substantial enhancement in the stiffness. Zafar [23] studied the impact of microwave power on the hole characteristics of microwave-drilled kenaf/PP composites. The results showed a non-linear growth in the hole diameter as the microwave power increased. Tirlangi et al. [24] explored the effect of different reinforcements (glass fiber and CNTs) on the mechanical properties of virgin recycled PP composites. Glass fiber significantly increased the tensile strength from 22.6 to 47.3 MPa, while CNTs enhanced the flexural strength from 56.8 to 68.4 MPa in neat-recycled PP.

Jan et al. [25] produced composite specimens using green wood-based fillers in both virgin and recycled PP matrices and examined their tribological behavior. The results showed distinct variations in the coefficient of friction (COF), and the wear rates in the recycled PP composites were notably lower than in virgin PP composites. Gorbe et al. [26] explored nanoparticle embedding in PP matrix-formed composite foams, revealing significant mechanical property improvements with an increased nanoparticle content. The tensile strength and Young's modulus notably increased (e.g., tensile strength rose from 3.2 MPa for the neat PP foam to 6.7 MPa with added nanoparticles). Leong et al. [27] studied the mechanical behavior of PP embedded with talc fillers and cellulose fibers in hybrid composites, reporting an increase in the neat PP's tensile strength from 30 to 50 MPa with these reinforcing agents. Ahmed et al. [28] developed PP embedded with waste tire-based composites, where they found an increased hardness from 60 Shore A for pure PP to 80 Shore A with the incorporation of waste tire rubber. Anandakumar et al. [29] fabricated a PP matrix embedded with short/continuous fibers via injection molding and conducted a low-velocity impact test. The impact strength of neat PP was 12.5 J, while the composite specimens exhibited higher impact strengths, ranging from 18 to 31 J, depending on the fiber reinforcement type and the proportion. Balogun et al. [30] developed a PP matrix embedded with jute and tetracarpidium conophorum composites, demonstrating an increase in the neat polypropylene's tensile strength from 28 to 50 MPa, indicating a significant enhancement in the tensile performance. Basilia et al. [23] investigated the impact of $CaCO_3$ on thermoplastic polymers, including polypropylene (PP), polyethylene (PE), and polyvinyl chloride (PVC). Their findings indicated that incorporating 3 wt.% $CaCO_3$ improved the properties; however, there was minimal improvement beyond this concentration. Therefore, in this study, a fixed amount of 2 wt.% $CaCO_3$ was employed, and the variation was solely focused on the GNPs loading. In addition, 5 wt.%

PP-MAH was used in this work as a non-reactive compatiblizer [15]. Previously, several researchers attempted to develop PP based composites reinforced with a single filler. However, polymeric composites embedded with more than one filler is expected to undergo a more positive hybrid effect obtained from two different fillers or matrices. In this work, $CaCO_3$ with 2 wt.% as primary filler was fixed based on previous literature [23]; additionally, the presence of $CaCO_3$ in polymer could improve mechanical properties of pipes and high resistance to external blow [31]. GNPs were chosen as secondary variable fillers with the PP matrix to enhance the service temperature and the mechanical and thermal properties [32].

Polypropylene is preferred in various applications such as automotive, packaging, medical, and industrial sectors due to its durability, chemical resistance, and insulation properties. However, it lacks in low-velocity impact strength and thermal stability. By introducing GNPs loading (0.5%–2%) along with PP-MAH and calcium carbonate, we aimed to enhance the thermal stability, low-velocity impact strength, and mechanical properties of PP. Hoorieh Barangizi et al. [33] dispersed either the 10 or 2 wt.% of PP using the solvent xylene in a flask, which was heated to 130 °C to prepare partially disentangled PP samples. After 1 h, the solution's temperature dropped at a rate of 25 °C/h. The solution became turbid due to gel formation when it reached 80 °C. The gel was taken out of the flask and allowed to dry at 40 °C. The dispersed aluminum oxide nanoparticles prevented the migration of macromolecules to the developing crystals, which slowed the crystallization in the nanocomposite compared to the homopolymer.

Melt mixing is the process most frequently used to create PP-nanocomposites. Shear pressure causes the PP to melt in a processing device (such as an internal mixer or twin-screw extruder) and distribute the nanotubes uniformly during the melt mixing process [34]. When it comes to melt compounding, mechanical equipment is mostly used to disperse the GNP throughout the PP melt. This is an economical, effective, and eco-friendly technology that is most suitable for industrialized manufacturing.

In the case of thermoset materials such as epoxy, the nanofillers were incorporated after heating the nanofiller (nano-alumina) from 80–120 °C for a specified time in an oven and then was mechanically blended followed by ultrasonication [35]. Ghabezi et al. [36] fabricated epoxy composites using glass fibers and varied the alumina Alpha and Gamma grade nano-alumina percentages. According to the experimental results, adding additional nanoparticles lengthened the filling time as they increased the fluid's viscosity and made it more resilient to the vacuum pressure applied to the fluid flow through preformed porous media. Epoxy nanocomposites were prepared by dispersing chemically functionalized reduced graphene oxide-polyaniline (rmGO-PANI) in chloroform by stirring at 1000 rpm. At 40 °C, the solvent chloroform was evaporated before the addition of hardener. Then, the rmGO-PANI-ES nanocomposites were coated on the mild steel samples [37]. The difficulty in the direct addition of graphene in a small weight percentage into the epoxy resin was overcome by first dispersing the graphene in ethanol solvent, followed by the epoxy resin addition using mechanical stirring. The final mixture was casted into PTFE mold after ultrasonication [38]. The functionalized graphene using polydopamine and reduced graphene oxide were dispersed in an ethanol solution, followed by ultrasonication and casting [39].

Some fascinating characteristics of GnPs include its low weight, high aspect ratio, mechanical durability, low cost, electrical and thermal conductivity, and planar structure. The authors [40,41] described the agglomeration and dispersion problems when GNPs were loaded as 3 % in PP and HDPE. Hence, in this research work, the highest GNP loading was fixed as 2%. The major problem of incorporating GNPs was its poor dispersion in non-polar polymers. This can be accomplished by

including either a compatibilizer or a functional modification of graphene during the fabrication process. Thus, the compatibilizer PP grafted maleic anhydride was incorporated along with GNP in the ethanol solution to facilitate the dispersion of GNP in a PP matrix. However, an unaddressed gap exists in research concerning PP matrices embedded with $CaCO_3$ and ultra-fine GNP-based hybrid composites. PP/CaCO₃/GNPs hybrid composites were prepared using 2 wt.% of $CaCO_3$ and different weight percentages of GNPs (0, 0.5, 1.0, 1.5, and 2.0 wt.%) via a twin-screw extrusion, followed by injection molding. Our primary focus was to investigate the influence of GNP loading on the mechanical and thermal properties of PP/CaCO₃/GNPs hybrid composites, aiming to enhance the low-velocity impact strength and thermal stability of PP. Through TGA and DSC characterization, we observed an increase in the corresponding thermal properties as the GNP loading was increased. Furthermore, the reinforcement effect of GNPs and $CaCO_3$ enhanced the low-velocity impact strength of PP/CaCO₃/GNPs hybrid composites. The tensile, compression, and flexural properties of samples with 0.5, 1.0 and 1.5 wt.% showed improvements due to the uniform dispersion of GNPs, thus facilitating an effective load transfer between the PP matrix and GNPs fillers. However, these properties decreased in the sample with a 2 wt.%. Overall enhanced mechanical and thermal properties were obtained for PP/2CC/GNPs-1.0 hybrid composites.

2. Materials and methods

2.1. Materials

PP homopolymer (Granules: 2.5–3.5 mm, SABIC, Saudi Arabia) was utilized as the base polymer, with a density of 0.92 g/cm^3 and a melt flow index is 7 g/10 min. The compatibilizer, PP-MAH (NG2002 grade) and $CaCO_3$ (0.64 μm) were commercially sourced in the Saudi market (Riyadh). The GNPs, in a dry powder form, with an average diameter of 5 μm and a thickness of 8 nm, were purchased from M/s Nanografi, Çankaya/Ankara, Turkey, with a purity exceeding 99.9%. In Figure 1a–c, the HR-SEM microstructure illustrates the distinct layers of the as-received GNPs [42]. Additionally, Figure 1d presents the schematic diagram of the hexagonal arrangement of the GNPs.
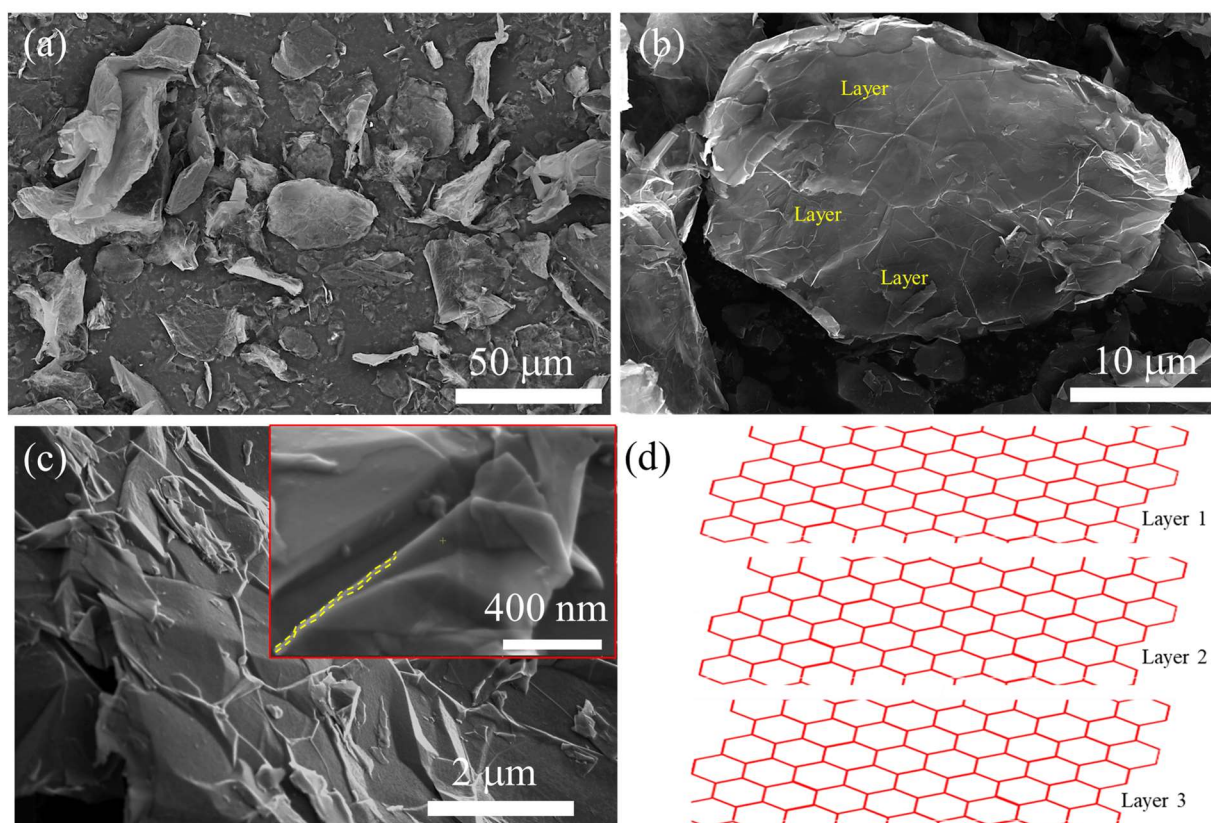
Figure 1. (a–c) HR-SEM micrograph of as-received GNPs at different magnifications, inset of (c) shows the thickness of GNP; (d) schematic diagram representing the arrangement of atoms in GNPs as hexagonal topography.

2.2. Development of PP/CaCO₃/GNPs hybrid composites

The as-received PP matrix granules, PP-MAH granules, $CaCO_3$, and GNPs underwent drying in an oven at 80 °C for 1 h to eliminate the moisture content. Different weight percentages of GNPs (0, 0.5, 1.0, 1.5, and 2.0 wt.%) and 2.0 wt.% of $CaCO_3$ were used to reinforce the pure PP matrix along with the compatibilizer. The material's composition, sample ID, and reinforcement percentages are detailed in Table 1. All materials were mechanically blended for approximately 45 min to achieve homogenization. Mechanical blending was carried out using a blender (M/s PHILIPS Hand mixer), which introduces mechanical forces on charged raw materials by a stirring action. The mechanical actions help to evenly distribute the materials throughout the polymer matrix, thus ensuring a uniform dispersion. During mechanical blending, the graphene nanoplates were expected to interact with the polymer matrix, thus forming strong interfacial bonds that enhanced the mechanical properties of the composite material. Before this, compatibilizers and GNPs were dispersed in ethanol (concentration of ethanol: materials ratio: 100: 15) using a magnetic stirrer (1000 mL capacity, LKTC-B1-T, KATLY, China) for 30 min to minimize the GNPs' agglomeration over the PP matrix. Then, the mixture was dried in an oven at 353 K for 2 h. Mechanically blended base PP, PP-MAH, $CaCO_3$, and GNPs were processed in a twin-screw extruder (screw diameter: 21 mm, input voltage: 220V, power: 1.1 kW, output range: 100–3000 g/h, production linear speed: <1000 cm/min, machine size: 1800 × 200 × 1000 mm, made: M/s Dongguan Junxin Plastic & Metal Co. Ltd., Qiaotou Town, Dongguan, China) for melt

compounding. The temperatures of three heating zones in the extrusion process were set as 195 ± 2 °C, 205 ± 2 °C, and 215 ± 2 °C, respectively [18]. A screw speed of 80 rpm was maintained during extrusion. Figure 2 illustrates the schematic diagram of the twin-screw extrusion process to prepare the granules, followed by a vertical injection molding machine (30 Ton capacity, supplied by M/s Dongguan Junxin Plastic & Metal Co. Ltd., Qiaotou Town, Dongguan, China) to fabricate the test specimens used for testing various mechanical properties such as the tensile, compressive, flexural, and impact resistances. The vertical injection molding machine barrel was covered with three heating zones using band heaters. The set temperatures in three zones were 200 ± 2 °C, 210 ± 2 °C, and 220 ± 2 °C, respectively.

Table 1. Sample designation, sample ID, percentage of PP, GNPs, CaCO$_3$, and PP-MAH.

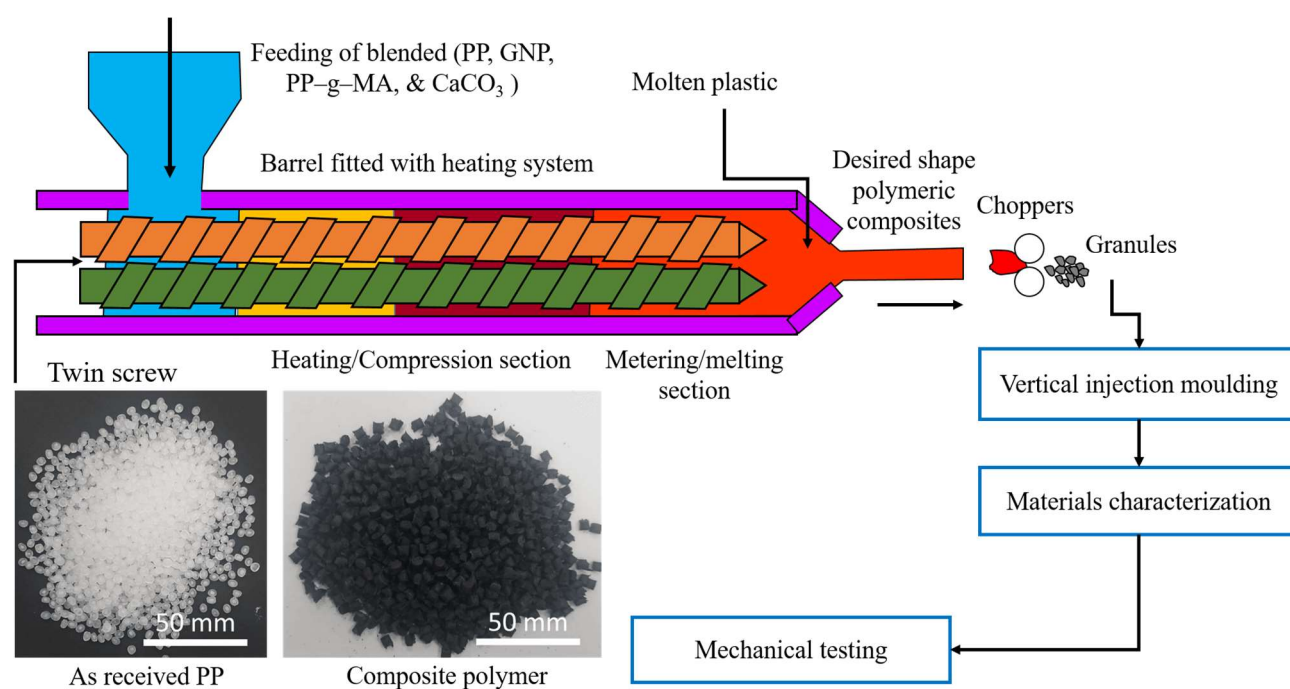| Sample designation	Sample ID	PP, wt.%	GNPs, wt.%	CaCO$_3$, wt.%	PP-MAH, wt.%
PP	PP/2CC/GNPs-0	100	-	-	-
PP+0.5GNP+2CaCO$_3$+5PP-MAH	PP/2CC/GNPs-0.5	92.5	0.5	2	5
PP+1GNP+2CaCO$_3$+5PP-MAH	PP/2CC/GNPs-1.0	92	1	2	5
PP+1.5GNP+2CaCO$_3$+5PP-MAH	PP/2CC/GNPs-1.5	91.5	1.5	2	5
PP+2GNP+2CaCO$_3$+5PP-MAH	PP/2CC/GNPs-2.0	91	2	2	5

Figure 2. Schematic diagram representing the present research work, including twin screw extrusion, pelletizing, vertical injection molding, materials characterization, mechanical testing, and photographs of developed hybrid composite granules.

2.3. Characterization of developed PP/CC/GNPs hybrid composites

FTIR, DSC, TGA, XRD, XPS and FEG-HRSEM analyses were carried out for the PP/2CC/GNPs-0, PP/2CC/GNPs-1.0, and PP/2CC/GNPs-2.0 hybrid composites. The FTIR analysis, which was conducted to identify chemical compounds, was conducted following the ASTM E168-16 standard [24], covering a wavelength range of 4000 to 380 cm^{-1} using a JASCO BSA spectrometer with a 4 cm^{-1} resolution. DSC analyses of PP/CC/GNP hybrid composite samples covered a temperature range from 27 to 550 °C, utilizing a heating rate of 10 °C/min under a N$_2$ atmosphere. A NETZSCH DSC 204 F1 thermal analyzer was employed following ASTM 3418 standards [24]. The samples were cooled to room temperature at 10 °C/min under nitrogen. Specimens weighing approximately 10 mg were prepared with precision to ensure flatness and smoothness for accurate DSC runs. Thermal properties, including change in enthalpy of melting (ΔH_m), degree of crystallinity (X_c), crystallization temperature (T_c), and melting temperature (T_m), were calculated using Eq 1 based on the melting enthalpy results.

$$\% \text{ Crystallinity, } X_c = \frac{\Delta H_m}{f \times \Delta H_m^\circ} \tag{1}$$

Here, f denotes the weight fraction of the PP matrix phase. The reference value for the enthalpy of 100% crystalline PP, denoted as ΔH_m°, is fixed at 209 J/g [43].

For the TGA, a M/s TA instrument (New Castle, DE, USA) was employed. The sample underwent heating from 25 to 700 °C, with a heating rate of 10 °C/min, under a nitrogen atmosphere. Essential TGA parameters, including the onset temperature, were derived from the TGA data, thus representing the temperature when the initial weight loss commenced. The XRD analysis was performed to examine different phases within the hybrid polymer composites. PANalytical X'Pert Pro instrument with Cu-Kα radiation was used to scan from a 5 to a 90° diffraction angle at a speed of 2°/min. XPS (Kα surface analysis, M/s Thermo Fisher Scientific, Altrincham, Cheshire, U.K) analyzed the elemental composition and chemical properties of the samples, thus providing insights into the overall structure. A sample size of around 10 × 10 × 10 mm was used for XPS examination. For FEG-HRSEM, an Apreo instrument was employed to assess the surface characteristics and fracture surfaces of samples subjected to mechanical testing, including the tensile and impact tests. The operational voltage was 30 keV, and the resolution was 1.3 nm.

2.4. Mechanical Properties of PP/CC/GNPs hybrid composites

Tensile tests, following ASTM D638 (Figure 3a), were conducted using a universal testing machine (M/s MTS System Corporation, model No: 370.25, 250 kN capacity, Texas, USA). Mechanical properties, including yield strength, ultimate strength, and elongation at rupture, were determined with a loading rate of 1 mm/min. Each material composition underwent five trials, and the average values were used for interpretation. Tensile stress (σ_t) was calculated using Eq 2:

$$\sigma_t = \frac{F_t}{A} \tag{2}$$

where F_t represents the applied tensile load (N) and A is the specimen's cross-sectional area (mm²).

The tensile strain (ε_t) was determined by Eq 3:

$$\varepsilon_t = \frac{\delta}{L} \tag{3}$$

where δ signifies deformation (mm) and L is the initial length of the specimen (mm).

Flexural testing, according to the ASTM D790 standard (Figure 3b), utilized the same MTS universal testing machine with a special fixture. The sample had a span of 40 mm between the supports, and the load was applied at the center. The flexural stress, flexural strain, and flexural modulus were determined with a testing speed of 1 mm/min. Each material composition underwent five trials in this test. The flexural stress (σ_b) was calculated using Eq 4:

$$\sigma_b = \frac{8FL}{\pi d^3} \tag{4}$$

where F is the bending load (N), L is support distance (mm), and d is the bending sample diameter (mm). The flexural strain (ε_b) was determined using Eq 5 while considering deflection (δ) at the span center (mm):

$$\varepsilon_b = \frac{6\delta d}{L^2} \tag{5}$$

The flexural modulus (E_b) was calculated via Eq 6, utilizing the first linear slope (m) from the bending force-deflection curve (between 0.25 Fmax and 0.75 Fmax) [44].
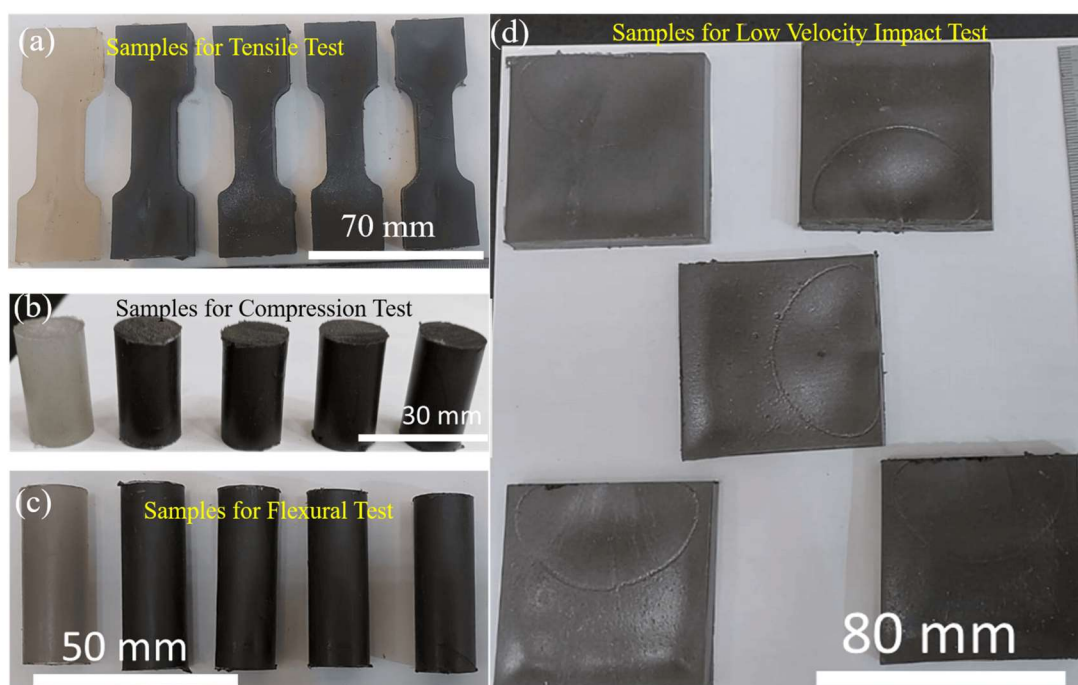
$$E_b = \frac{4L^3 m}{3\pi d^4} \tag{6}$$

Figure 3. Photographs of fabricated samples for mechanical testing of: (a) tensile samples; (b) compressive samples; (c) 3P bending test samples; and (d) low-velocity impact test samples.
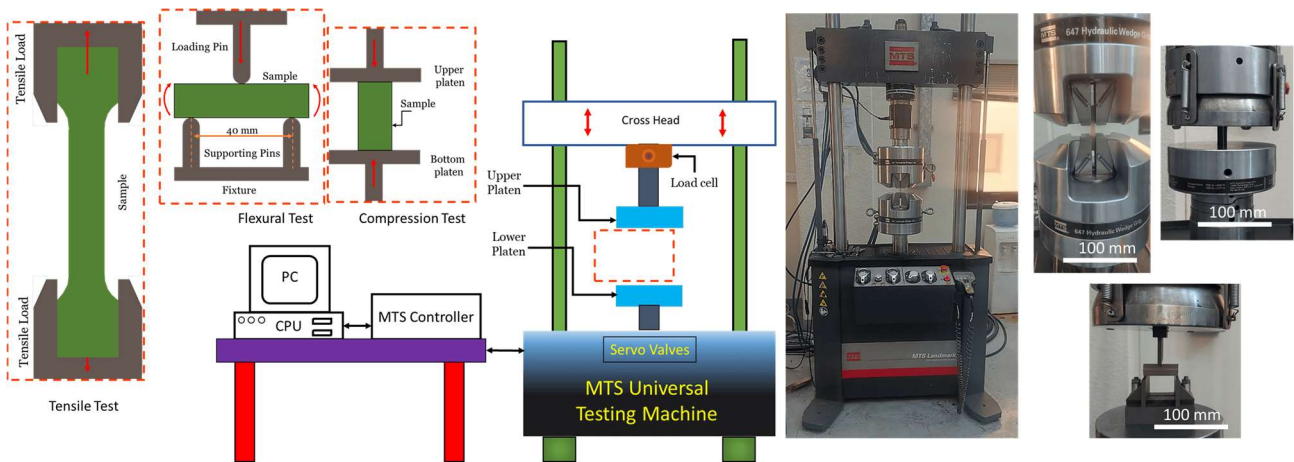
Figure 4. Schematic diagram showing various mechanical testing (tensile, flexural, and compressive) using MTS universal testing machine, photograph of MTS machine and magnified photos showing samples under different types of loadings.

The uniaxial compression test, following the ASTM D695 standard (Figure 3c), utilized a 15 mm diameter and a 22.5 mm length specimen. At least five trials were conducted for each composition. The compressive stress (σ_c) was determined using Eq 7:

$$\sigma_C = \frac{F_C}{A} \tag{7}$$

where Fc is the applied compressive load (N) and A is the cross-sectional area of the specimen (mm²). The compressive strain (ε_c) was calculated with Eq 8:

$$\sigma_C = \frac{F_C}{A} \tag{8}$$

with δ representing deformation (mm) and L is the initial length of the specimen (mm).

Similarly, the low-velocity impact test (LVI), adhering to ASTM D7136 standard (Figure 3d), used 60 mm square samples with a 10 mm thickness. Figure 4 illustrates the schematic diagram of various mechanical tests (tensile, flexural, and compressive) performed on an MTS universal testing machine, including a photograph of the MTS machine and magnified photos showing samples under different loading conditions.

Figure 5 presents the schematic diagram of the low-velocity impact test conducted on an INSTRON CEAST 9350 machine (M/s INSTRON CEAST factory, 90 Ton capacity, Milan city, Italy), including a photograph of the machine and magnified photos showing samples under the impact load. The peak impact force, absorbed impact energy, velocity, and displacement profiles were computed using Eqs 9–11 [45,46]:

$$v(t) = v_i + \int_0^t \frac{F(t)}{m} dt \tag{9}$$

$$D(t) = D_i + v_i t + \frac{gt^2}{2} - \int_0^t \left(\int_0^t \frac{F(t)}{m} \right) dt \tag{10}$$

$$E(t) = \frac{m[v_i^2 - v(t)^2]}{2} + mgD(t) \tag{11}$$

where v is the velocity in m/s, v_i is the incident velocity of the impactor in m/s, t is the time in ms, g is the gravity in m/s^2, F(t) is the vertical force in N, m is the mass in kg, D(t) is the displacement in mm, and D_i is the initial position in mm.
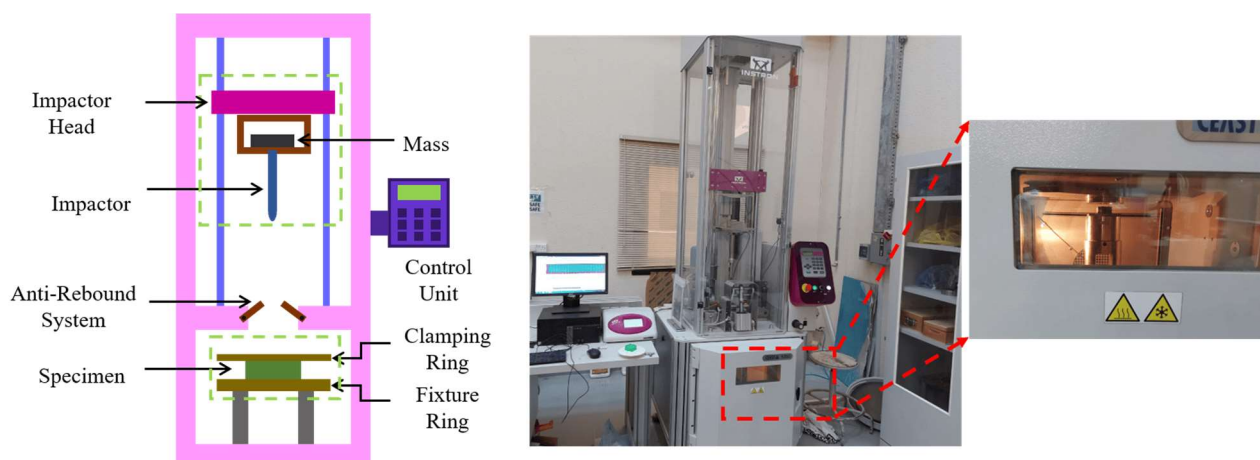

Figure 5. Schematic diagram showing low velocity impact test in a drop tower testing machine, photograph of INSTRON CEAST 9350 machine and magnified photos showing samples under impact load.

3. Results and discussion

3.1. Characterization of Morphological Features using FEG-HRSEM

The dispersion of GNPs and $CaCO_3$ within the PP matrix was examined through high resolution SEM (HRSEM) using a cross-sectioned injection-molded sample, as shown in Figure 6. HRSEM morphological analyses revealed an average size of agglomerated GNPs at 6 ± 21 μm with a thickness of 5 nm. Figure 6a displays the HRSEM topography of the pure PP matrix, showing a clean and increased PP domain. Figure 6b depicts the presence of a slightly reduced PP domain, indicating an interfacial tension between incorporated GNPs and $CaCO_3$ with the PP matrix [15]. As shown in Figure 6c–e, with an increase in GNP loading, the observed PP domain started to decrease due to the large interfacial tension of the PP matrix with the GNPs and $CaCO_3$, thus confirming the effective compatibilization effect given by PP-MAH. This was attributed to the increased viscosity of the PP matrix and the barrier effect produced by the GNPs and $CaCO_3$. Furthermore, the presence of GNPs and $CaCO_3$ over the PP matrix domain confirmed the proper bonding of embedded GNPs and $CaCO_3$ with the PP matrix. However, as per Figure 6e, a non-uniform distribution of GNPs over the PP matrix occurred, and an increased agglomeration of GNPs and $CaCO_3$ occurred in a higher loading of GNPs, which may be expected to decrease the mechanical properties. HRSEM-BSE elemental mapping and EDS analyses of PP/2CC/GNP-1.0 hybrid composite polymer are shown in Figure 7 with insets presenting the observed elemental composition. The presence of the microstructure (Figure 7a), carbon (Figure 7b), oxygen (Figure 7c), and calcium (Figure 7d) in the hybrid composites (Figure 7e,f) indicates successful compounding of the incorporated compatibilizers along with the GNPs [22] during the processing of the incorporated GNPs and $CaCO_3$ fillers [47,48].
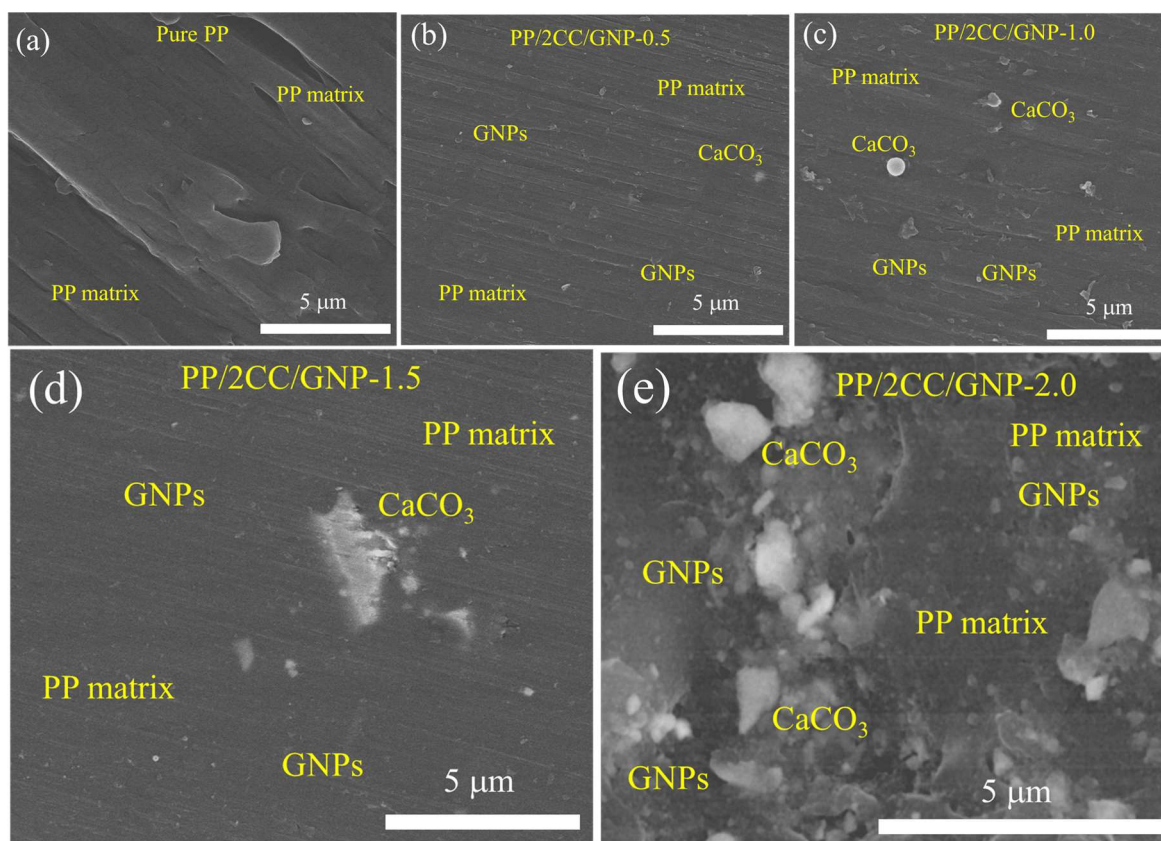
Figure 6. (a–e) HRSEM cross-sectional analyses of injection molded samples of: (a) pure PP matrix; (b) PP/2CC/GNP-0.5; (c) PP/2CC/GNP-1.0; (d) PP/2CC/GNP-1.5; (e) PP/2CC/GNP-2.0 hybrid composites.
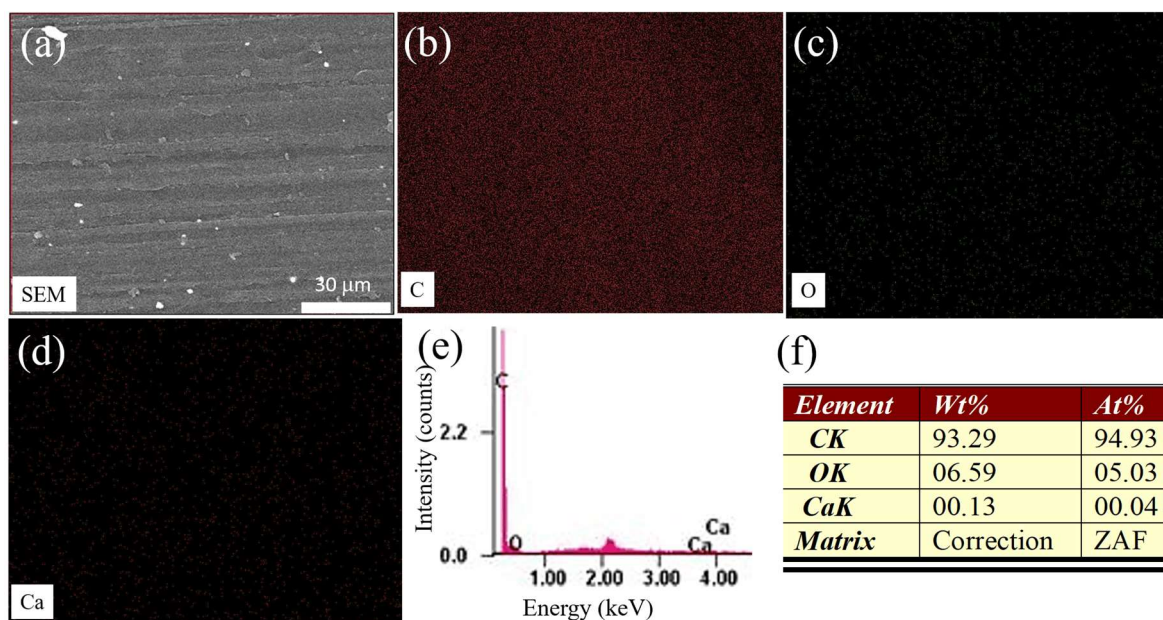

Element	Wt%	At%
CK	93.29	94.93
OK	06.59	05.03
CaK	00.13	00.04
Matrix	Correction	ZAF

Figure 7. (a–e) HRSEM-BSE elemental mapping of PP/2CC/GNP-1.0 hybrid composites: (a) microstructure, (b) carbon, (c) oxygen, (d) calcium, and (e,f) EDS result of (a).

3.2. Investigation of crystalline structure via XRD analysis

Figure 8 presents the XRD peak profiles of the pure PP matrix, PP/2CC/GNPs-1.0, and PP/2CC/GNPs-2.0 hybrid composite polymers. In the pure PP matrix, the XRD peaks centered at 2θ angles of 14.3, 16.7, 18.7, 22.6, and 25.4° were observed, corresponding to (110), (040), (130), (202), and (060) planes, respectively, and associated with the α-form of the PP matrix crystals. No additional peaks or oxides were noticed, indicating purity and a process capability. The XRD profiles of the hybrid composites at a 2θ angle of 26.4 and 26.8° were related to the incorporated $CaCO_3$ and GNPs, with the corresponding plane being (104) and (002), respectively. The results demonstrate a decrease and broadening of the PP matrix crystal peaks with the addition of ultra-fine GNPs, and the peak corresponding to GNPs increased with their content, thus confirming successful composite formation. The peak positions of the α-form PP matrix shifted with an increase in the GNPs loading. This shift was attributed to the large interfacial tension between the incorporated GNPs and the PP matrix. This significant interfacial tension occurs due to the increasing viscosity of the PP matrix with the addition of GNPs. Niu et al. [47] and Xie et al. [49] reported that the addition of a PP-MAH compatibilizer in the PP matrix could suppress the formation of the β-form of the PP crystals. Therefore, in the present XRD results, no β-form of the PP crystals was observed. The relative amount of GNPs in the PP matrix, represented by a factor (K), was determined by the ratio of the XRD peak intensity of GNPs (IGNPS) at (002) to the sum of intensities of the α-form PP matrix crystals ($I_{\alpha1}$, $I_{\alpha2}$, $I_{\alpha3}$, and $I_{\alpha4}$) at four different diffraction angles of (110), (040), (130) and (202), respectively, calculated using the following Eq 12 [47,49]:

$$K = \frac{I_{GNPs}}{(I_{\alpha1}+I_{\alpha2}+I_{\alpha3}+I_{\alpha4}+I_{GNPs})} \tag{12}$$

The calculated K values were 0 for the pure PP matrix, 0.10 for the PP/2CC/GNPs-1.0 hybrid composite and 0.16 for the PP/2CC/GNPs-2.0 hybrid composite. The K value signifies GNP crystal formation, with PP/2CC/GNPs-2.0 showing a higher K value, thus indicating more GNPs crystals in this sample. This result confirms the successful development of the composite.
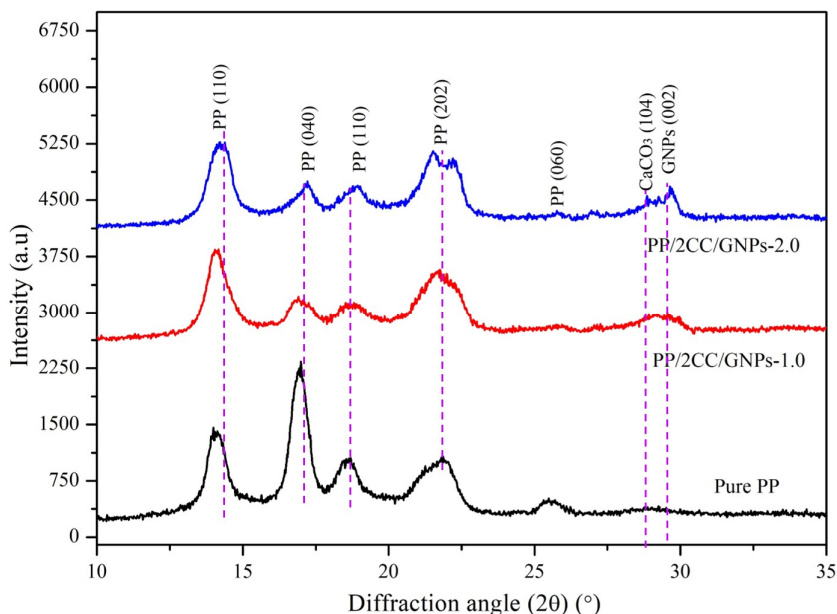
Figure 8. XRD profiles of pure PP matrix, PP/2CC/GNPs-1.0, and PP/2CC/GNPs-2.0 hybrid composites.

3.3. Examination of chemical properties through XPS analysis

Figure 9 illustrates the XPS profiles of the pure PP matrix, PP/2CC/GNPs-1.0 hybrid composite, and PP/2CC/GNPs-2.0 hybrid composite, thus elucidating the chemical nature and composition. The atomic concentrations of various elements present in the developed polymers are detailed in Table 2. The XPS survey scanning (Figure 9) indicates an increased peak intensity of C1s with rising GNPs (0 to 2 wt.%), thus signifying the successful development of composites. Conversely, the O1s peak intensity decreased with escalating GNPs, thus confirming proper bonding and nucleation of GNPs in the PP matrix [50,51]. Detailed peak deconvolution was examined in the XPS results at the C1s and O1s levels, as illustrated in Figures 10 and 11, respectively (Table 3). At the C1s level, three de-convoluted peaks at 282, 283, and 284 eV represented CHn/C–C (alkyl group [52,53], C–OH (alcoholic group [53]), and C=O (alkyl group [54]). The increase in alkyl (CHn/C–C) and alcoholics (C–OH) peaks with rising GNPs confirms effective bonding in the polymer chain. At the O1s level (Figure 11), peaks at 533 and 535 eV represented the carboxylic acid group (O=C–O) and ketone group (O=C) [44], which are associated with nucleation and bonding effects; this increased with higher GNP content, affirming the successful formation of hybrid composites.
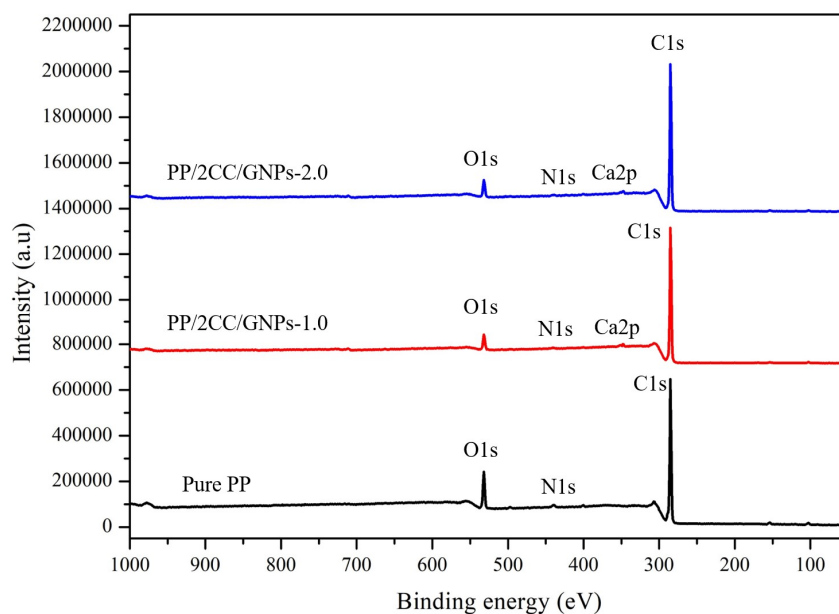
Figure 9. X-ray photoelectron spectroscopy (XPS) of pure PP matrix, PP/2CC/GNPs-1.0 and PP/2CC/GNPs-2.0 hybrid composites.

Table 2. Chemical composition of different elements in the developed pure PP matrix, PP/2CC/GNPs-1.0 and PP/2CC/GNPs-2.0 hybrid composites were measured using XPS.

Name of sample	Atomic concentrations, %		
	C1s	O1s	Ca2p
Pure PP matrix	86.89	13.11	-
PPGNPs-1.0	88.62	10.26	1.12
PPGNPs-2.0	92.49	6.61	0.9

Table 3. XPS peak position for the corresponding observed C1s, and O1s of developed pure PP matrix, PP/2CC/GNPs-1.0 and PP/2CC/GNPs-2.0 hybrid composites.

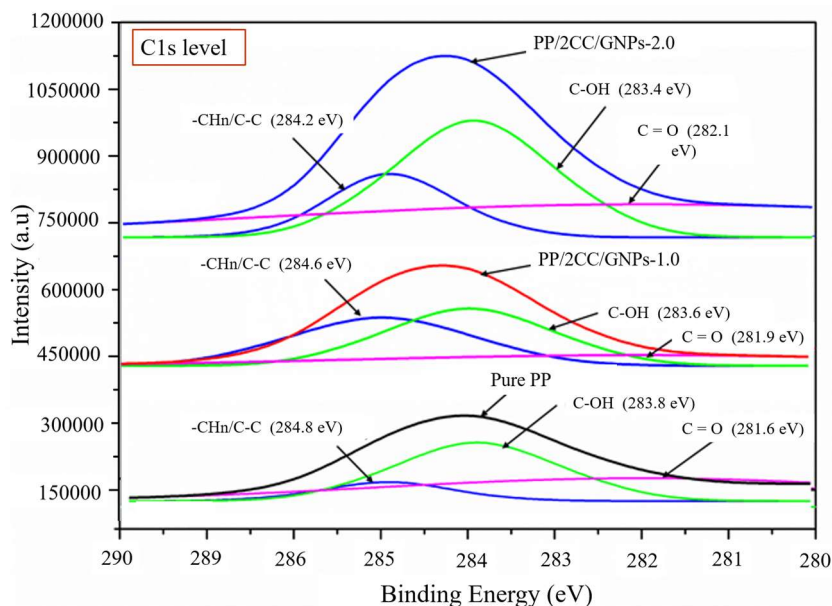| Binding energy (eV)	C1s			O1s			Ca2p
	–CHn/C–C	C–OH	C=O	C=O	O=C–O		CaCO$_3$
	Alkyl group	Alcoholics group	Ketone group	Ketone group	carboxylic acid group		
HEP0Gr	284.8	283.8	281.6	535.3	533.6		-
HEP1.0Gr	284.6	283.6	281.9	535.5	533.7		350.0
HEP2.0Gr	284.2	283.4	282.1	535.7	533.8		350.1

Figure 10. XPS spectra examined at the center of C1s level for pure PP matrix, PP/2CC/GNPs-1.0 and PP/2CC/GNPs-2.0 hybrid composites.
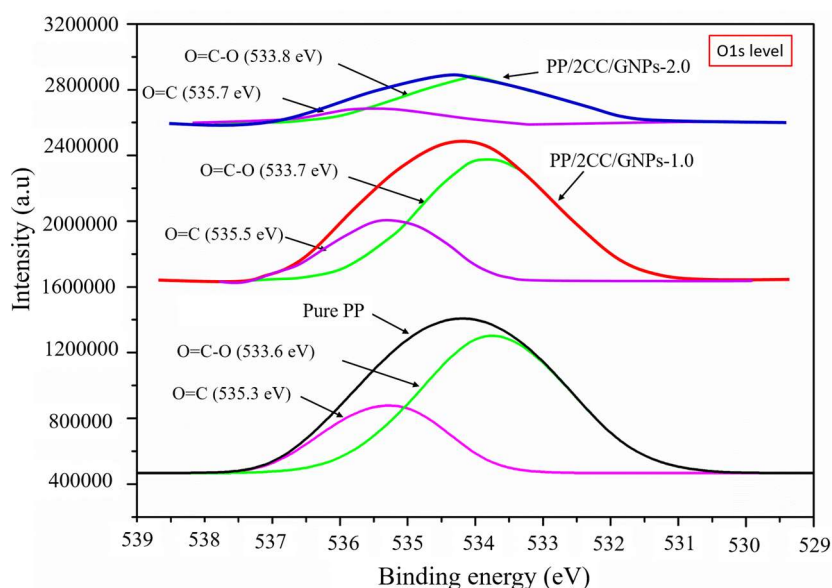

Figure 11. XPS spectra examined at the center of O1s level for pure PP matrix, PP/2CC/GNPs-1.0 and PP/2CC/GNPs-2.0 hybrid composites.

3.4. Evaluation of molecular structure using FTIR analysis

The molecular formation and bonding structure of the as-received GNPs, the developed pure PP matrix, PP/2CC/GNPs-1.0 hybrid composite, and PP/2CC/GNPs-2.0 hybrid composite were examined using FTIR, as depicted in Figure 12. For as-received GNPs (Figure 12a), the observed peaks at 3438 and 2923 cm^{-1} are related to stretching of the O–H bond, whereas, the observed peaks at 1731, 1635,

and 1075 cm^{-1} are attributed to stretching vibrations of C=C, C–OH, and C=O, respectively [55,56]. For the developed composites (Figure 12b), asymmetric vibrations within the wavelength range of 2903–2945 cm^{-1} (point A) and symmetric vibrations within 2815–2962 cm^{-1} (point B) confirm the copolymer nature and robust bonding of incorporated GNPs in the PP matrix [57,58]. The range of 2903–2945 cm^{-1} (point A) corresponds to asymmetric stretching vibrations of the CH$_3$ group of the PP matrix [58]. The range of 2815–29625 cm^{-1} (point B) indicates symmetric stretching vibrations, corresponding to the CH$_2$ group of the PP matrix. The observed peak depth at point A increases with GNPs up to 1 wt.% in the PP matrix (PP/2CC/GNPs-1.0), then decreases in PP/2CC/GNPs-2.0, signifying alterations in the internal structure and the occurrence of compounding due to nucleation and strong bonding of the incorporated GNPs in the PP matrix [56] (Figure 12c). At 1380 cm^{-1} (point C), umbrella bending vibrations indicate C–H bonds in all samples; at 1460 cm^{-1} (point D), symmetrical bending vibrations corresponding to the CH$_3$ group are present. These FTIR results confirm the successful development of hybrid composites.
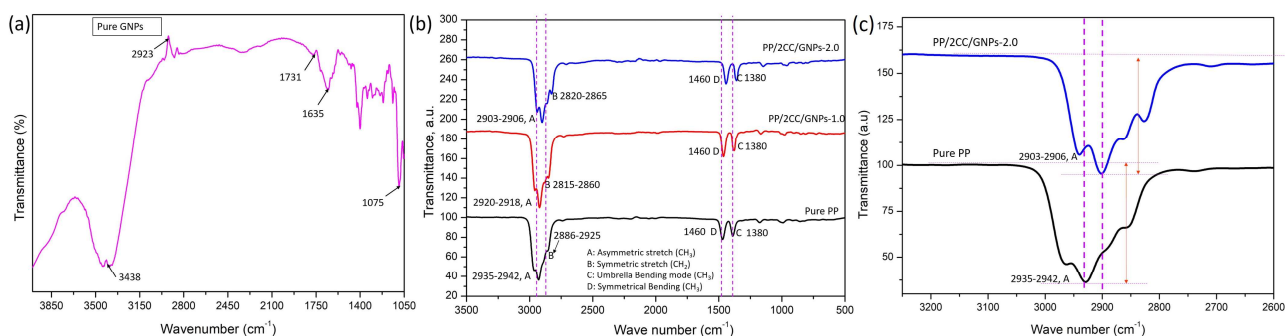

Figure 12. FTIR profile of (a) as-received pure GNPs; (b) developed pure PP matrix, PP/2CC/GNPs-1.0 and PP/2CC/GNPs-2.0 hybrid composites; (c) magnified view of (b).

3.5. Assessment of thermal properties via DSC analysis

Figure 13a illustrates the DSC analysis of the developed hybrid composites (pure PP, PP/2CC/GNP-1.0, and PP/2CC/GNP-2.0) during heating (Figure 13b) and cooling (Figure 13c) cycles. The thermal properties, including the Tc, Tm, change in enthalpy of recrystallization (ΔHc), ΔHm, crystallinity at room temperature, and percentage of Xc, were determined, as listed in Table 4.

The results demonstrate that incorporating GNPs into the PP matrix significantly influences the thermal properties. For the pure PP matrix polymer, the calculated ΔHm and ΔHc were 52.43 and −26.15 J/g, respectively. In contrast, the PP/2CC/GNP-2.0 hybrid composite exhibited a ΔHm and ΔHc of 74.01 and −40.48 J/g, respectively. The PP/2CC/GNP-1.0 hybrid composite showed a 16.4% increased ΔHm and a 31.2% increased ΔHc compared to the pure PP matrix, while PP/2CC/GNP-2.0 exhibited a 41.11% increased ΔHm and a 54.76% increased ΔHc. These results indicate varied thermal properties with the incorporation of GNPs into the PP matrix. Additionally, the percentage of crystallinity significantly increased with the addition of GNPs, attributed to effective bonding between the GNPs and PP, resulting in the formation of more α-PP crystals. The introduction of GNPs caused a noteworthy change in the melting temperature (Tm, increased from 166.2 to 172.1 °C) and the recrystallization temperature (Tc, decreased from 124.8 to 118.6°), highlighting the strong bonding

effect of GNPs with the α-PP matrix [59]. The observed decrease in the Tc and the increase in Tm can be attributed to the presence of GNPs and $CaCO_3$ in the composites. The decrease in the Tc might be associated with a hindrance of the crystallization process caused by the presence of GNPs and $CaCO_3$, which could act as nucleation sites and could affect the overall crystallization kinetics. An increase in the Tm could be related to changes in the crystalline structure induced by the interaction between PP and the incorporated fillers [59].
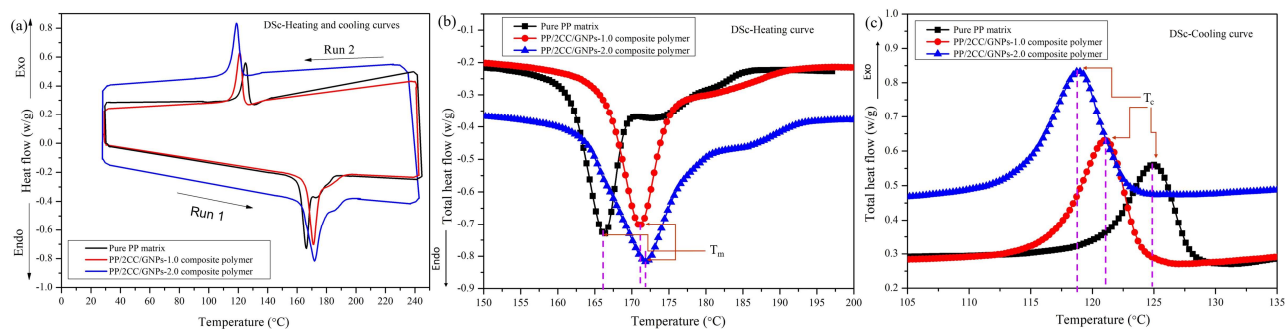

Figure 13. DSC curves of developed pure PP matrix, PP/2CC/GNP-1.0 and PP/2CC/GNP-2.0 hybrid composites of: (a) combined heating and cooling curves; (b) magnified view of heating curve; (c) magnified view of cooling curve.

Table 4. Thermal properties obtained from DSC results for the developed hybrid composites.

Name of sample	Tc, °C	ΔHc, J/g	Tm, °C	ΔHm, J/g	$\sum(\Delta Hc + \Delta Hm)$, J/g	Xc
Pure PP matrix	124.8	−26.159	166.2	52.430	26.271	25.086
PP/2CC/GNPs-1.0	121.2	−34.520	171.4	61.013	26.492	30.095
PP/2CC/GNPs-2.0	118.6	−40.486	172.1	74.016	33.530	36.889

3.6. Analysis of thermal stability using TGA analysis

Figure 14 displays the thermal degradation profiles of the developed pure PP matrix, PP/2CC/GNPs-1.0 hybrid composite, and PP/2CC/GNPs-2.0 hybrid composite. This provides insights into the thermal stability of all developed samples. The calculated thermal degradation temperatures at different weight loss percentages (5%, 10%, 20%, and 50%) are listed in Table 5. Examining Figure 14 and Table 5 reveals a substantial improvement in the thermal stability with the incorporation of GNPs compared to the pure PP matrix, as attributed to the strong nucleating and bonding effects of GNPs over the PP matrix. For instance, the onset temperature on the weight loss of pure PP matrix at $T_{5\%}$, $T_{10\%}$, $T_{20\%}$, and $T_{50\%}$ was 371.89, 406.49, 433.99, and 460.35 °C, respectively. In contrast, the onset temperature on weight loss of the PP/2CC/GNP-2.0 hybrid composite at $T_{5\%}$, $T_{10\%}$, $T_{20\%}$, and $T_{50\%}$ was 388.02, 422.81, 444.36, and 466.40 °C, respectively. The enhanced thermal stability in the PP/2CC/GNPs hybrid composite can be attributed to the insulating and barrier effects of the introduced GNPs, thus leading to an increased thermal resistance compared to the pure PP matrix [18]. At a maximum temperature of 500 °C, the residual weight of the pure PP matrix, PP/2CC/GNPs-1.0 hybrid composite, and PP/2CC/GNPs-2.0 hybrid composite were found to be 0%, 1.5%, and 2.45%,

respectively. These results indicate an improvement in the thermal stability of the GNPs-loaded hybrid composites.

Table 5. TGA of developed pure PP matrix, PP/2CC/GNPs-1.0 and PP/2CC/GNPs-2.0 hybrid composites listing the degradation temperature with the function of weight loss.

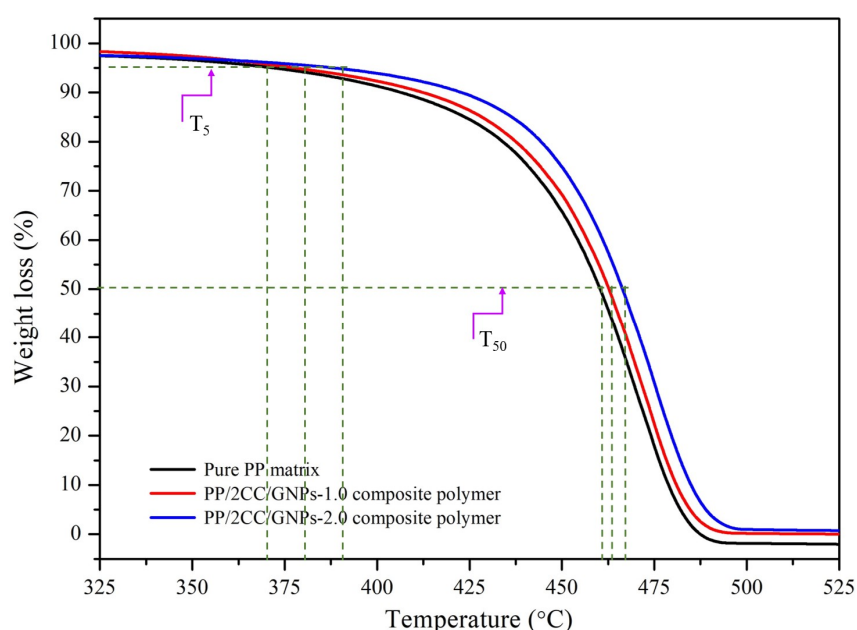| Name of sample	Thermal degradation temperature, (°C)			
	Weight loss at 5%, T_5 (°C)	Weight loss at 10%, T_{10} (°C)	Weight loss at 20%, T_{20} (°C)	Weight loss at 50%, T_{50} (°C)
Pure PP matrix	371.89	406.49	433.99	460.34
PP/2CC/GNPs-1.0	377.61	412.37	437.53	462.72
PP/2CC/GNPs-2.0	388.02	422.81	444.36	466.40

Figure 14. TGA of pure PP matrix, PP/2CC/GNPs-1.0 and PP/2CC/GNPs-2.0 hybrid composites.

3.7. Evaluation of mechanical properties

3.7.1. Tensile testing

The mechanical properties, including the yield strength, strain at the yield point, ultimate strength, strain at the ultimate point, fracture strength, strain at fracture, modulus of elasticity, and toughness, were evaluated via tensile testing using engineering stress-strain curves, depicted in Figure 15. Corresponding mechanical properties are detailed in Figure 16. The results unmistakably reveal a substantial increase in the tensile strength of the pure PP matrix with an escalating percentage of GNPs. For example, the ultimate tensile strength of the pure PP matrix, PP/2CC/GNPs-0.5, PP/2CC/GNPs-1.0, PP/2CC/GNPs-1.5, and PP/2CC/GNPs-2.0 was 35.829, 37.474, 40.076, 40.546, and 38.426 MPa,

respectively. The enhanced tensile strength compared to the pure PP matrix was 4.59%, 11.85%, 13.16%, and 7.25% for PP/2CC/GNPs-0.5, PP/2CC/GNPs-1.0, PP/2CC/GNPs-1.5, and PP/2CC/GNPs-2.0, respectively. This improvement is attributed to the nucleating effect of GNPs in the PP matrix, proper bonding of the incorporated GNPs, and a uniform dispersion of GNPs, thereby facilitating an effective load transfer between the PP matrix and GNPs fillers [18,60]. As depicted in Figure 16, there is a notable decrease in the tensile strain at the ultimate point, with an increasing content of GNPs in the PP polymer matrix, which is attributed to an escalation in defects upon the introduction of GNPs. For instance, the percentage reduction in the tensile strain for developed hybrid composite polymers compared to pure PP matrix was 19.23%, 23.07%, 25.64%, and 34.65% for PP/2CC/GNPs-0.5, PP/2CC/GNPs-1.0, PP/2CC/GNPs-1.5, and PP/2CC/GNPs-2.0, respectively. This outcome signifies a substantial reduction in the elongation/ductility, indicating a hindered chain mobility within the polymer matrix due to the increased GNPs content in the PP matrix. Consequently, this results in a heightened stiffness in the composites, aligning with previously reported findings in the literature [18,61].
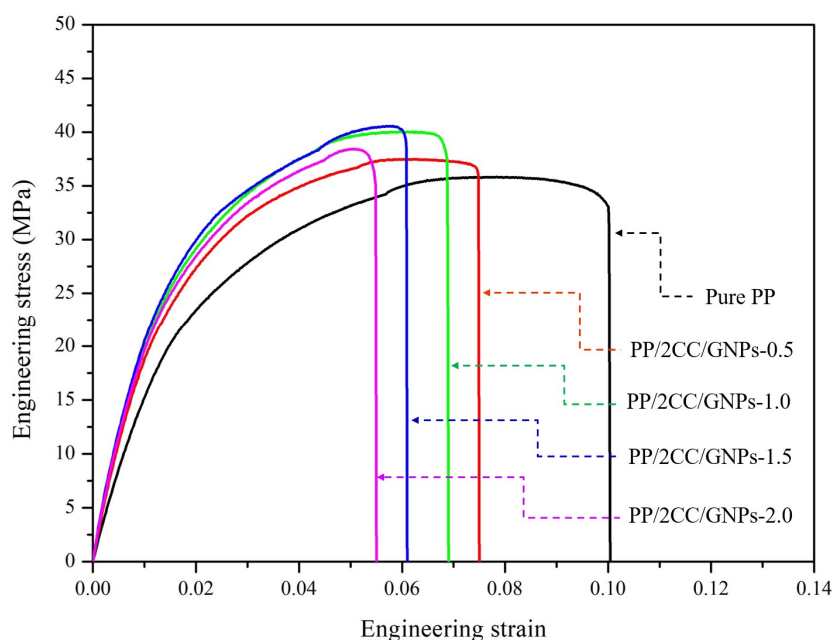

Figure 15. Engineering stress-strain curves of pure PP matrix, PP/2CC/GNPs-0.5, PP/2CC/GNPs-1.0, PP/2CC/GNPs-1.5, and PP/2CC/GNPs-2.0 hybrid composites obtained from uniaxial tensile test.
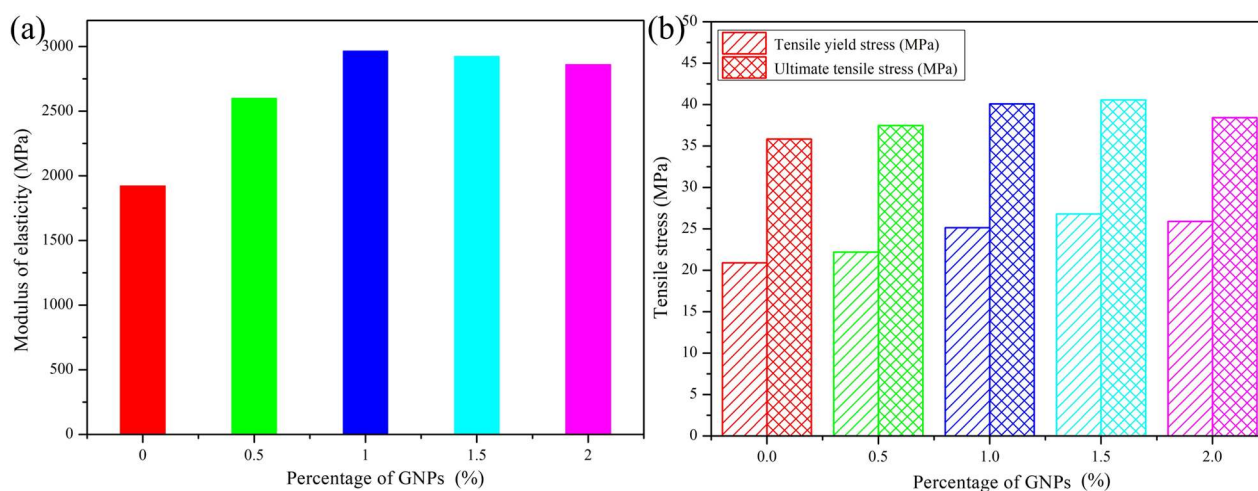
Figure 16. Mechanical properties (a) modulus of elasticity; (b) tensile yield stress and ultimate tensile stress of developed pure PP matrix, PP/2CC/GNPs-0.5, PP/2CC/GNPs-1.0, PP/2CC/GNPs-1.5, and PP/2CC/GNPs-2.0 hybrid composites.

3.7.2. Compression testing

An analysis of the mechanical properties from a compression test, including the compressive yield strength, the compressive strain at the yield point, the ultimate compressive strength, and the compressive strain at the ultimate point, was conducted through engineering compressive stress-strain curves. Upon analyzing Figures 17 and 18, it's clear that the compressive strength of the hybrid composites significantly increases with the GNPs incorporation into the pure PP matrix. For example, the percentage improvement in the ultimate compressive strength compared to the pure PP matrix was 9.75%, 14.44%, 21.27%, and 16.57% for PP/2CC/GNPs-0.5, PP/2CC/GNPs-1.0, PP/2CC/GNPs-1.5, and PP/2CC/GNPs-2.0, respectively. The compressive strength depends on factors such as the compatibility between polar and nonpolar components in the polymer blend. The observed enhancement (Figures 17 and 18) is attributed to the nucleating effects of the GNPs in the PP matrix, an effective dispersion, and load transfer between GNPs and PP matrix. Additionally, the introduced percentage of $CaCO_3$ and PP-MAH may have contributed to an improvement in the compressive properties during the uniaxial compressive test. PP/2CC/GNPs-1.5 demonstrated the highest mechanical properties among the developed hybrid composites. The mechanical properties started to decrease beyond 1.5%, leading to the decision to stop the addition of GNPs at 2.0%.
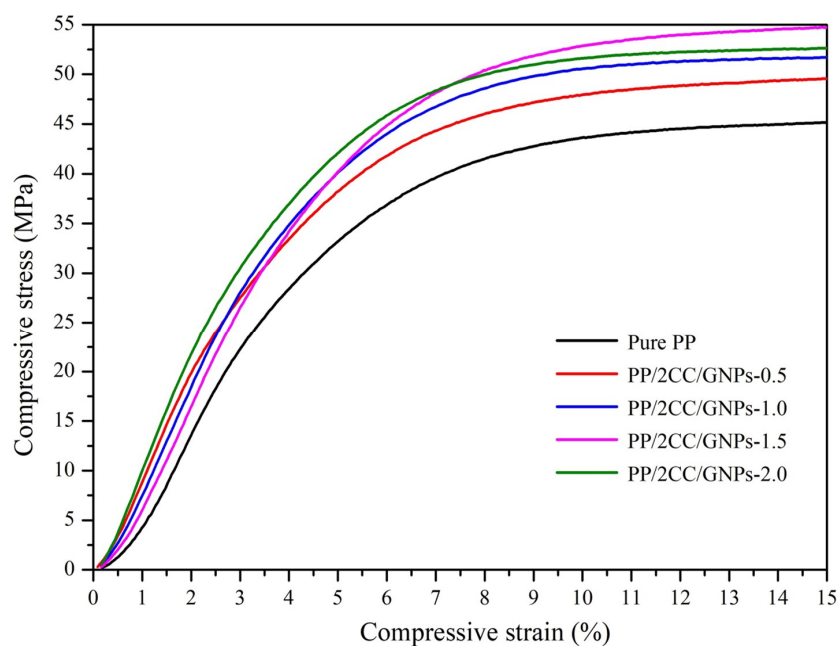
Figure 17. Compressive stress-strain curves of pure PP matrix, PP/2CC/GNPs-0.5, PP/2CC/GNPs-1.0, PP/2CC/GNPs-1.5, and PP/2CC/GNPs-2.0 hybrid composites obtained from uniaxial compression test.
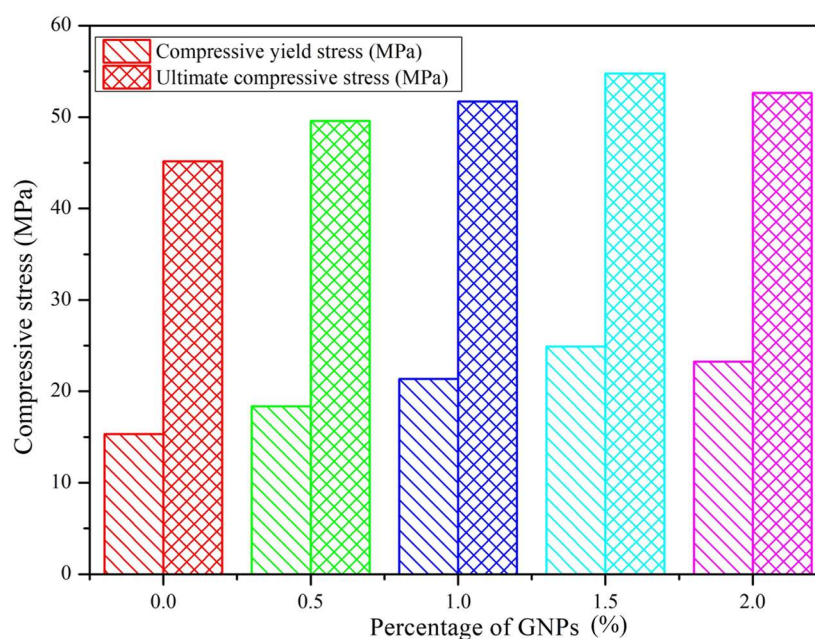

Figure 18. Compressive properties of developed pure PP matrix, PP/2CC/GNPs-0.5, PP/2CC/GNPs-1.0, PP/2CC/GNPs-1.5, and PP/2CC/GNPs-2.0 hybrid composites.

3.7.3. Flexural testing

The flexural properties, including the flexural stress, strain, modulus, and toughness, were determined through a three-point bending test. These properties, derived from engineering flexural

stress-strain curves (Figure 19). Reviewing the results in Figures 19 and 20 reveals a substantial increase in the flexural strength for the PP/2CC/GNPs-based hybrid composite with GNPs incorporation. This improvement is attributed to an effective GNP interaction with the PP matrix, a uniform GNP dispersion, and the barrier effect of GNPs, along with other factors described earlier.
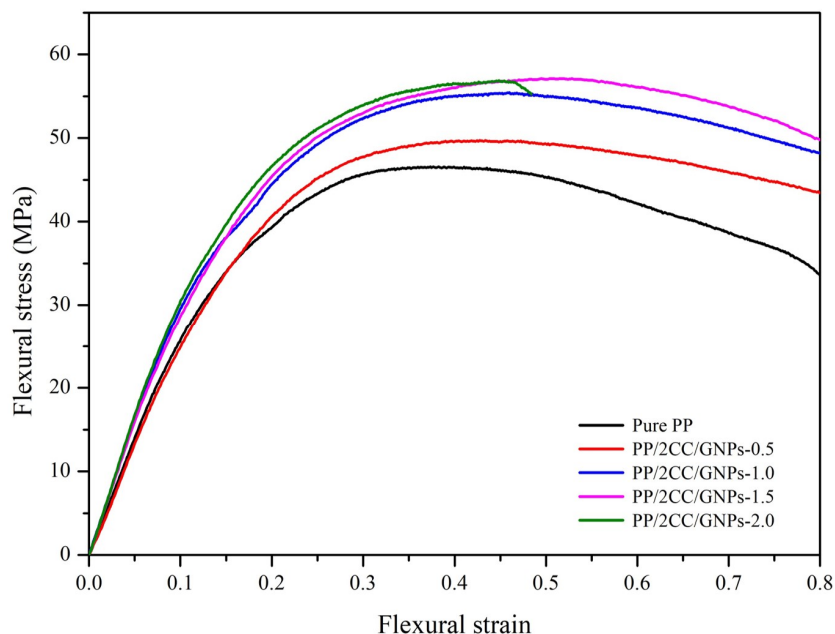

Figure 19. Flexural stress-strain curves of pure PP matrix, PP/2CC/GNPs-0.5, PP/2CC/GNPs-1.0, PP/2CC/GNPs-1.5, and PP/2CC/GNPs-2.0 hybrid composites obtained from 3P bending test.
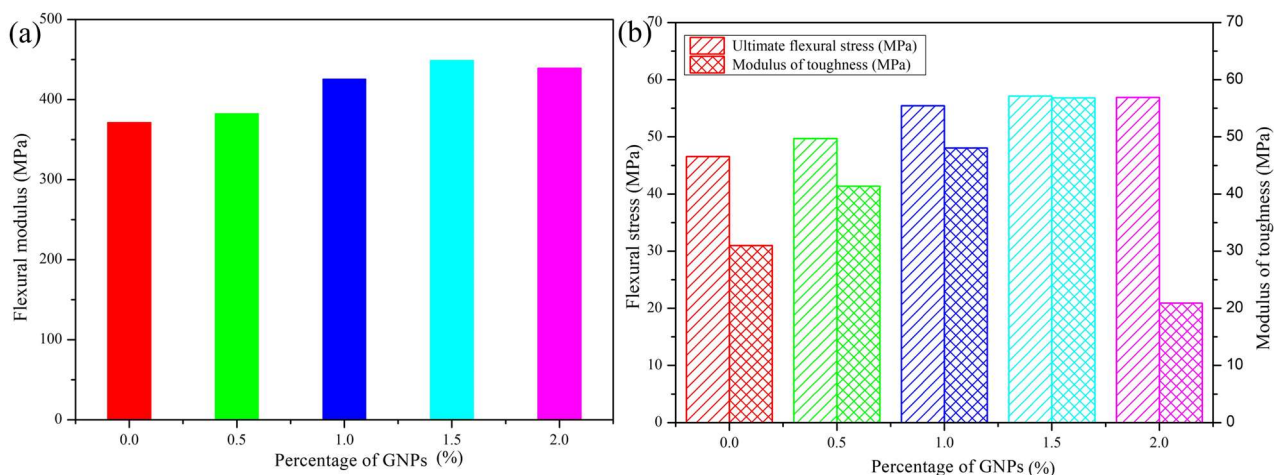

Figure 20. Flexural properties. (a) Flexural modulus and (b) flexural stress and modulus of toughness of developed pure PP matrix, PP/2CC/GNPs-0.5, PP/2CC/GNPs-1.0, PP/2CC/GNPs-1.5, and PP/2CC/GNPs-2.0 hybrid composites.

3.7.4. Low velocity impact test

Low-velocity impact testing aimed to evaluate the impact performance of the newly developed composites using a CEAST 9350 Instron impact testing machine (Figure 5). This machine is comprised of a weight dropping system with an impactor head housing the insert, an anti-rebound mechanism, a lubrication system, a photocell, and a high-energy configuration positioning system. A hemispherical impactor insert (40 mm length, 20 mm diameter) was employed. The testing chamber, which was maintained at room temperature, contained a specimen holder, a clamping mechanism, and a temperature control. The specimen was clamped with a pressure of 5.5 bars. The parameters for the low-velocity impact tests are detailed in Table 6. The impact velocity denotes the speed at which the impactor insert contacts the specimen surface. Based on the findings presented in Figure 21, it becomes evident that the peak impact force and the energy observed in the developed hybrid composites significantly increased with the incorporation of 2 wt.% $CaCO_3$/x wt.% GNPs. Furthermore, the residual velocity considerably decreased with an increased content of 2 wt.% $CaCO_3$/x wt.% GNPs in the PP matrix. The reasons for the improved impact properties were attributed to the nucleating effects of the incorporated GNPs in the PP matrix, strong interactions between the GNPs and $CaCO_3$ with the PP matrix, and an effective dispersion of the GNPs as discussed in an earlier section.
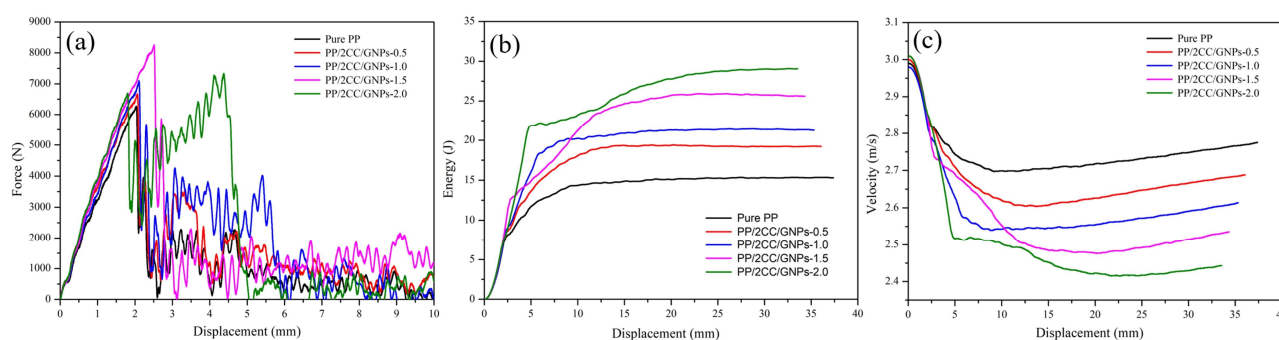

Figure 21. Low velocity behavior of pure PP matrix, PP/2CC/GNPs-0.5, PP/2CC/GNPs-1.0, PP/2CC/GNPs-1.5, and PP/2CC/GNPs-2.0 hybrid composites: (a) force Vs displacement profile; (b) energy Vs displacement profile; (c) velocity Vs displacement profile.

Table 6. Low-velocity impact testing parameters used in the testing of developed high-entropy polymers.

Parameter	Value	Parameter	Value
Applied impact energy	75 J	Insert diameter	20 mm
Impact velocity	3.11 m/s	Environmental temperature	20 ℃
Falling height	493 mm	Striker load capacity	90 KN
Impactor head mass	15.5 kg		

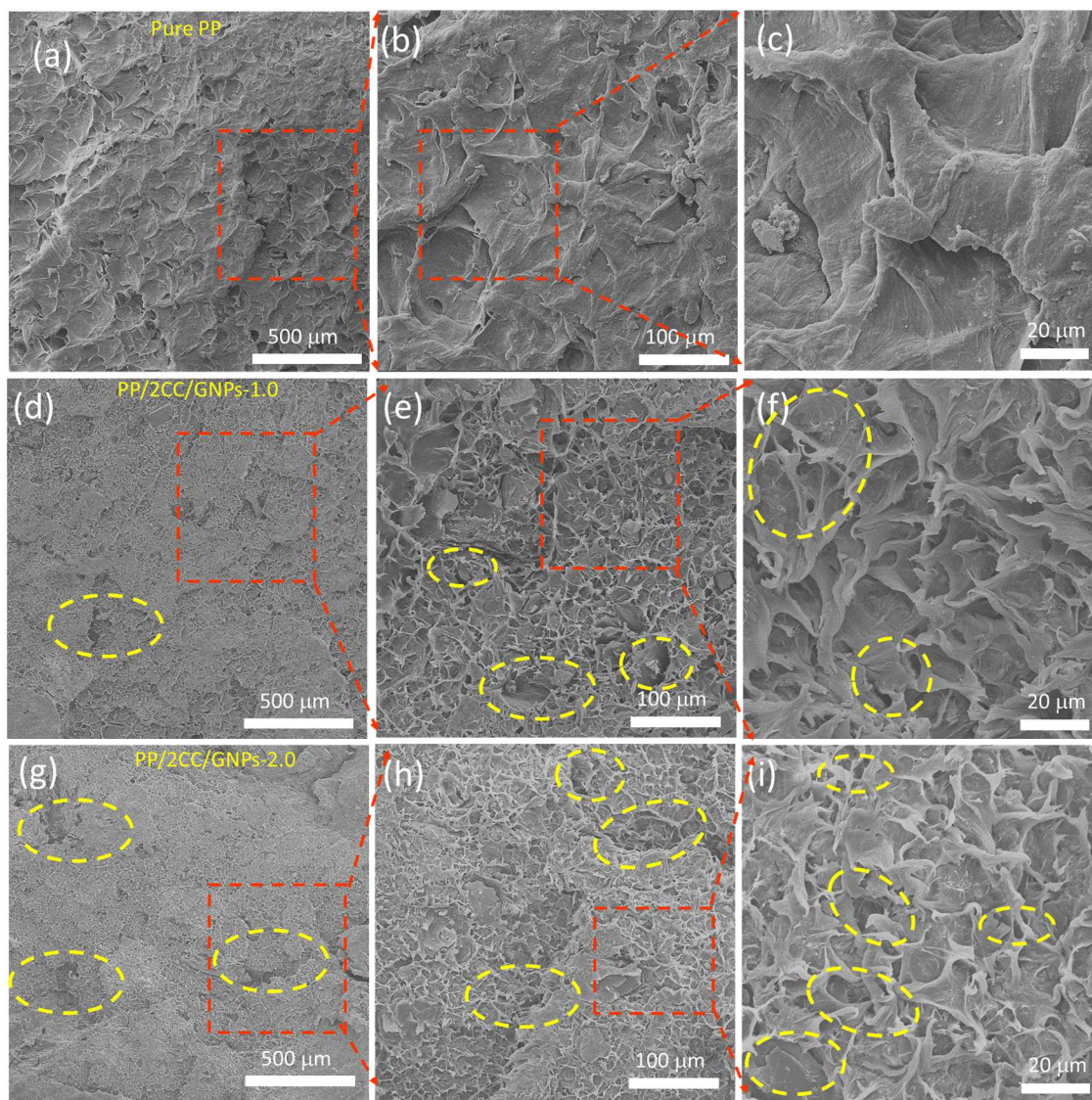## 3.8. Analysis of fracture surface topography

Figure 22. SEM microstructure of fractured area after tensile test of: (a–c) pure PP matrix; (d–f) PP/2CC/GNPs-1.0, and (g–i) PP/2CC/GNPs-2.0 hybrid composites. Yellow dashed circle represents the location of GNPs/CaCO$_3$ fillers over PP matrix.

A fracture surface analysis is a pivotal technique to study polymer hybrid composites, providing crucial insights into the behavior and failure mechanisms by examining the fractured surfaces post-mechanical testing. SEM microstructures after tensile and impact tests were captured and are depicted in Figures 22 and 23, respectively. Ductile SEM morphology with regular wave-like patterns characterized the pure PP matrix due to proper compounding [62] (Figure 22a–c). Notably, the pure PP matrix showed an absence of cracks, voids, and inclusions. In contrast, PP/2CC/GNPs-1.0 exhibited a rough surface with uniform GNPs pull-outs, indicating an effective load-transfer between the GNPs and CaCO$_3$ within the PP matrix (Figure 22d–f). However, PP/2CC/GNPs-2.0 showed a very rough surface with more voids, cracks, cleavage patterns, and non-uniform GNPs pull-outs due to agglomeration

and increased defects (Figure 22g–i), thus resulting in lower mechanical properties (Figures 16, 18 and 20). Beyond 1 wt.% of GNPs, the presence of more defects, cleavage patterns, and a non-uniform dispersion led to a brittle fracture behavior and deteriorating mechanical properties. Similarly, after the impact test, a homogeneous ductile fracture surface was obtained in the pure PP matrix (Figure 23a–c). PP/2CC/GNPs-1.0 showed a slightly rough surface with a brittle flat surface (Figure 23d–f), while PP/2CC/GNPs-2.0 exhibited a severely rough, completely brittle fracture surface with more damages (Figure 23g–i), thus indicating the presence of defects and a reduced bonding strength.
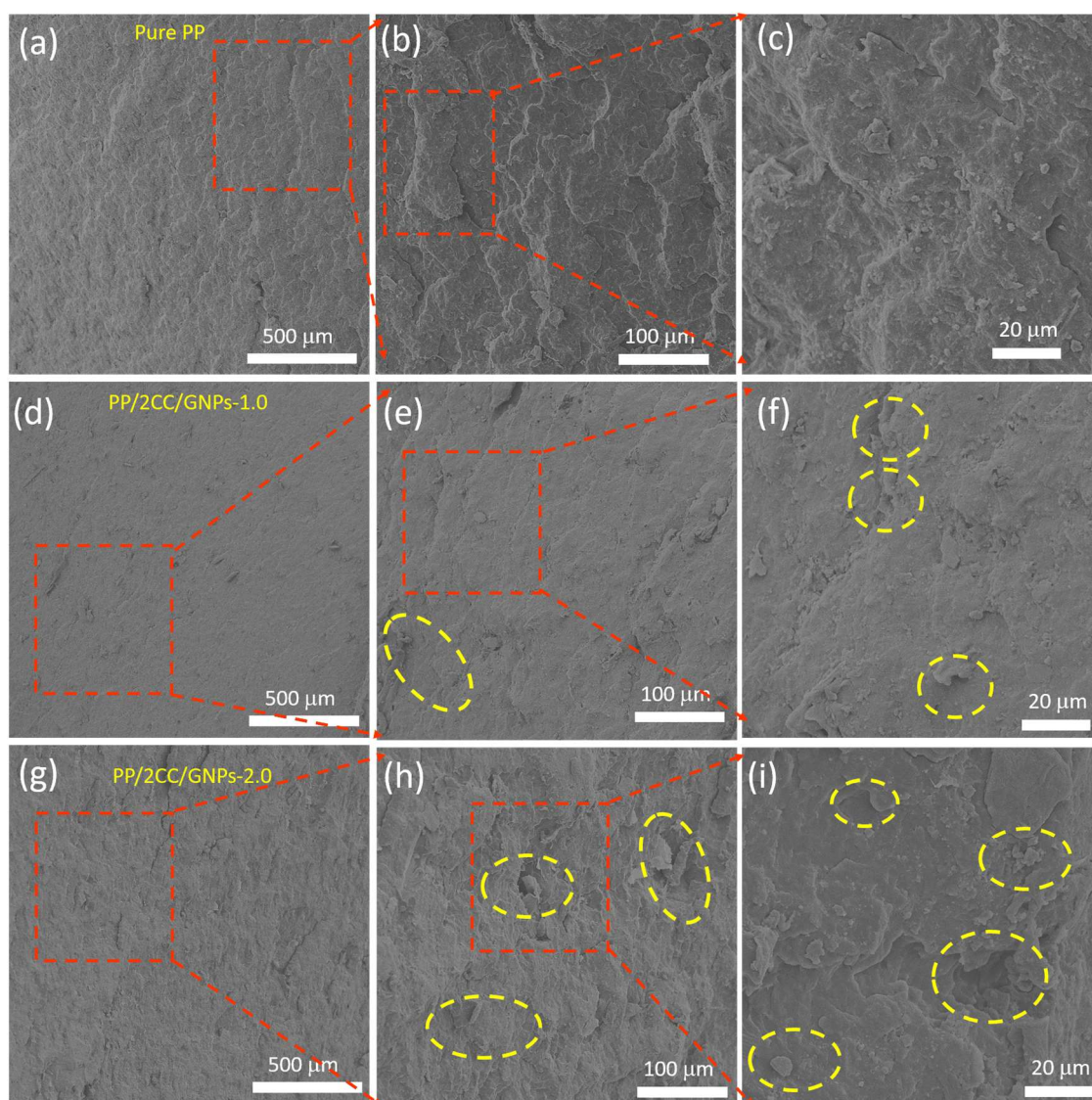

Figure 23. SEM microstructure of fractured area after impact test of: (a–c) pure PP matrix; (d–f) PP/2CC/GNPs-1.0, and (g–i) PP/2CC/GNPs-2.0 hybrid composites. Yellow dashed circle represents the location of GNPs/CaCO$_3$ fillers over PP matrix.

4. Conclusions

In this paper, the effect of $CaCO_3$ and different weight percentages of GNPs loading on the thermal and mechanical properties of PP were investigated. PP/$CaCO_3$/GNPs hybrid composites were prepared by melt compounding via a twin-screw extrusion. FTIR results confirmed the successful development of hybrid composites. FEG-HRSEM confirmed the purity and morphology of the synthesized hybrid composites due to the proper bonding of embedded GNPs and $CaCO_3$ within the PP matrix. A XRD analysis showed a higher K value for PPGNPs-2.0, thus indicating additional GNPs crystals. TGA and DSC characterizations revealed enhanced thermal properties. Due to the effective dispersion and bonding between reinforcements (GNPs and $CaCO_3$) and the PP matrix, the low velocity impact strength of PP/$CaCO_3$/GNPs hybrid composites was enhanced. Additionally, the tensile, compression, and flexural properties showed additional improvements with the increase in GNP loading. HRSEM fracture surface analyses revealed microstructural features, with PP/2CC/GNPs-1.0 showing improved characteristics compared to other hybrid composites. Based on the findings, the PP/2CC/GNPs-1.0 hybrid composite is recommended for structural and other applications due to its improved thermal and mechanical properties.

Use of AI tools declaration

The authors declare they have not used Artificial Intelligence (AI) tools in the creation of this article.

Author contributions

Conceptualization: D.B., R.K., S.S., A.E.; validation: D.B., R.K., S.S., B.S; formal analysis: D.B., A.A., R.K.; investigation: R.K., S.S., B.S., A.A.; resources: R.K., S.S., A.A.; data curation: R.K., S.S., B.S., A.A.; writing—original draft preparation: D.B., R.K., S.S., B.S., A.A., writing—review and editing: S.S., B.S., A.A.; supervision: R.K., S.S., B.S. All authors have read and agreed to the published version of the manuscript.

Conflicts of interests

The authors declare no conflict of interest.

Data availability statement

The experimental datasets obtained from this research work and then the analyzed results during the current study are available from the corresponding author upon reasonable request.

References

1. Hu P, Yang H (2013) Polypropylene filled with kaolinite-based conductive powders. *Appl Clay Sci* 83–84: 122–128. https://doi.org/10.1016/j.clay.2013.08.025

2. Cataldi P, Athanassiou A, Bayer IS (2018) Graphene nanoplatelets-based advanced materials and recent progress in sustainable applications. *Appl Sci* 8: 1438. https://doi.org/10.3390/app8091438

3. Potts JR, Dreyer DR, Bielawski CW, et al. (2011) Graphene-based polymer nanocomposites. *Polymer* 52: 5–25. https://doi.org/10.1016/j.polymer.2010.11.042

4. Geng Y, Li J, Wang SJ, et al. (2008) Amino functionalization of graphite nanoplatelet. *J Nanosci Nanotechnol* 8: 6238–6246. https://doi.org/10.1166/jnn.2008.18377

5. Inuwa IM, Hassan A, Samsudin SA, et al. (2014) Characterization and mechanical properties of exfoliated graphite nanoplatelets reinforced polyethylene terephthalate/polypropylene composites. *J Appl Polym Sci* 131: 40582. https://doi.org/10.1002/app.40582

6. Karevan M, Kalaitzidou K (2013) Formation of a complex constrained region at the graphite nanoplatelets-polyamide 12 interface. *Polymer* 54: 3691–3698. https://doi.org/10.1016/j.polymer.2013.05.019

7. Kalaitzidou K, Fukushima H, Drzal LT (2007) Mechanical properties and morphological characterization of exfoliated graphite–polypropylene nanocomposites. *Compos Part A Appl Sci Manuf* 38: 1675–1682. https://doi.org/10.1016/j.compositesa.2007.02.003

8. Duguay AJ, Nader JW, Kiziltas A, et al. (2014) Exfoliated graphite nanoplatelet-filled impact modified polypropylene nanocomposites: Influence of particle diameter, filler loading, and coupling agent on the mechanical properties. *Appl Nanosci* 4: 279–291. https://doi.org/10.1007/s13204-013-0204-2

9. Coleman JN, Khan U, Blau WJ, et al. (2006) Small but strong: A review of the mechanical properties of carbon nanotube–polymer composites. *Carbon* 44: 1624–1652. https://doi.org/10.1016/j.carbon.2006.02.038

10. Beloshenko VA, Voznyak AV, Voznyak Y, et al. (2017) Effect of simple shear induced orientation process on the morphology and properties of polyolefin/graphite nanoplates composites. *Compos Sci Technol* 139: 47–56. https://doi.org/10.1016/j.compscitech.2016.12.009

11. Vilaverde C, Santos RM, Paiva MC, et al. (2015) Dispersion and re-agglomeration of graphite nanoplates in polypropylene melts under controlled flow conditions. *Compos Part A Appl Sci Manuf* 78: 143–151. https://doi.org/10.1016/j.compositesa.2015.08.010

12. Jang BJ, Zhamu A (2008) Processing of nanographene platelets (NGPs) and NGP nanocomposites: A review. *J Mater Sci* 43: 5092–5101. https://doi.org/10.1007/s10853-008-2755-2

13. He FA, Wu HJ, Yang XL, et al. (2015) Novel exfoliated graphite nanoplates/syndiotactic polystyrene composites prepared by solution-blending. *Polym Test* 42: 45–53. https://doi.org/10.1016/j.polymertesting.2015.01.002

14. Paszkiewicz S, Taraghi I, Fereidoon A, et al. (2018) Nanocomposites based on polymer blends: Enhanced interfacial interactions in polycarbonate/ethylene-propylene copolymer blends with multi-walled carbon nanotubes. *Compos Interfaces* 25: 275–286. http://dx.doi.org/10.1080/09276440.2018.1393253

15. Ajitha AR, Mathew LP, Thomas S (2019) Effect of MA-g-PP compatibilizer on morphology and electrical properties of MWCNT based blend nanocomposites: New strategy to enhance the dispersion of MWCNTs in immiscible poly (trimethylene terephthalate)/polypropylene blends. *Eur Polym J* 118: 595–605. http://dx.doi.org/10.1016/j.eurpolymj.2019.06.027

16. Jolfaei AF, Gavgani JN, Jalali A, et al. (2015) Effect of organoclay and compatibilizers on microstructure, rheological and mechanical properties of dynamically vulcanized EPDM/PP elastomers. *Polym Bull* 72: 1127–1144. http://dx.doi.org/10.1007/s00289-015-1328-1

17. Yousfi M, Livi S, Dumas A, et al. (2014) Compatibilization of polypropylene/polyamide 6 blends using new synthetic nanosized talc fillers: Morphology, thermal, and mechanical properties. *J Appl Polym Sci* 131: 40453. https://doi.org/10.1002/app.40453

18. Al-Saleh MA, Yussuf AA, Al-Enezi S, et al. (2019) Polypropylene/graphene nanocomposites: Effects of GNP loading and compatibilizers on the mechanical and thermal properties. *Materials* 12: 3924. https://doi.org/10.3390/ma12233924

19. Wang S, Ajji A, Guo S, et al. (2017) Preparation of microporous polypropylene/titanium dioxide composite membranes with enhanced electrolyte uptake capability via melt extruding and stretching. *Polymers* 9: 110. https://doi.org/10.3390/polym9030110

20. Alaburdaite R, Paluckiene E, Grevys S (2016) Comparison of the surface characteristics of polyethylene and polypropylene films and polyester textile coated with electroconductive copper sulphide thin films. *Chalcogenide Lett* 13: 529–536.

21. Yang N, Zhang ZC, Ma N, et al. (2017) Effect of surface modified kaolin on properties of polypropylene grafted maleic anhydride. *Results Phys* 7: 969–974. http://dx.doi.org/10.1016/j.rinp.2017.02.030

22. Meena R, Hashmi AW, Ahmad S, et al. (2023) Influence of fly ash on thermo-mechanical and mechanical behavior of injection molded polypropylene matrix composites. *Chemosphere* 343: 140225. https://doi.org/10.1016/j.chemosphere.2023.140225

23. Rampal, Zafar S (2023) Effect of microwave power on the hole characteristics in microwave-drilled kenaf/polypropylene composites. *J Manuf Process* 102: 218–230. https://doi.org/10.1016/j.jmapro.2023.07.052

24. Tirlangi S, Mohamed MJS, Karthik K, et al. (2023) Influence on the mechanical properties of virgin recycled polypropylene composites with different types of reinforcing loads. *Mater Today Proc*. http://dx.doi.org/10.1016/j.matpr.2023.07.235

25. Jan P, Matkovic S, Bek M, et al. (2023) Tribological behaviour of green wood-based unrecycled and recycled polypropylene composites. *Wear* 524: 204826. https://doi.org/10.1016/j.wear.2023.204826

26. Gorbe A, Varga LJ, Barany T (2023) Development of nanoparticle-filled polypropylene-based single polymer composite foams. *Heliyon* 9: e19638. https://doi.org/10.1016/j.heliyon.2023.e19638

27. Leong YW, Abu Bakarm MB, Ishak ZAM, et al. (2004) Comparison of the mechanical properties and interfacial interactions between talc, kaolin, and calcium carbonate filled polypropylene composites. *J Appl Polym Sci* 91: 3315–3326. http://dx.doi.org/10.1002/app.13542

28. Ahmed KZ, Faizan M, Azam F, et al. (2023) Hardness assessment of novel waste tire rubber-polypropylene composite. *Mater Today Proc*. https://doi.org/10.1016/j.matpr.2023.03.445

29. Anandakumar P, Timmaraju MV, Velmurugan R (2023) Low-velocity impact behavior of injection over-molded short/continuous fiber reinforced polypropylene composites. *Mater Today Proc*. http://dx.doi.org/10.1016/j.matpr.2023.02.368

30. Balogun OA, Daramola OO, Adediran AA, et al. (2023) Investigation of Jute/Tetracarpidium conophorum reinforced polypropylene composites for automobile application: Mechanical, wear and flow properties. *Alex Eng J* 65: 327–341. http://dx.doi.org/10.1016/j.aej.2022.10.026

31. Rothon R, Paynter C (2017) Calcium carbonate fillers, In: Rothon R, *Fillers for Polymer Applications. Polymers and Polymeric Composites: A Reference Series*, Cham: Springer. https://doi.org/10.1007/978-3-319-28117-9_35

32. Prolongo SG, Moriche R, Jimenez-Suarez A, et al. (2014) Advantages and disadvantages of the addition of graphene nanoplatelets to epoxy resins. *Eur Polym J* 61: 206–214. https://doi.org/10.1016/j.eurpolymj.2014.09.022

33. Hoorieh B, Andrzej P (2022) Crystallization of partially disentangled polypropylene in nanocomposites with aluminum oxide. *Polymer* 254: 125049. https://doi.org/10.1016/j.polymer.2022.125049

34. Gorbe A, Varga LJ, Barany T (2023) Development of nanoparticle-filled polypropylene-based single polymer composite foams. *Heliyon* 9: e19638. https://doi.org/10.1016/j.heliyon.2023.e19638

35. Ghabezi P, Farahani M, Fakhr HM, et al. (2016) Investigation of mechanical behavior of alfa and gamma nano-alumina/epoxy composite made by Vartm. *Int J Adv Biotechnol Res* 7: 731–736.

36. Ghabezi P, Farahani M, Fakhr HM (2016) Experimental investigation of nano-alumina effect on the filling time in Vartm process. *J Fundam Appl Sci* 82S: 925–940. http://dx.doi.org/10.4314/jfas.v8i2s.146

37. Mourya P, Ramesh NG, Saini R, et al. (2024) Epoxy coating reinforced with graphene-PANI nanocomposites for enhancement of corrosion-resistance performance of mild steel in saline water. *Colloid Surface A* 687: 133500. http://dx.doi.org/10.1016/j.colsurfa.2024.133500

38. Feng J, Safaei B, Qin Z, et al. (2023) Effects of graphene surface morphology on damping properties of epoxy composites. *Polymer* 281: 126107. https://doi.org/10.1016/j.polymer.2023.126107

39. Feng J, Safaei B, Qin Z, et al. (2023) Nature-inspired energy dissipation sandwich composites reinforced with high-friction graphene. *Compos Sci Technol* 233: 109925. https://doi.org/10.1016/j.compscitech.2023.109925

40. Zhao X, Huang D, Ewulonu CM, et al. (2021) Polypropylene/graphene nanoplatelets nanocomposites with high conductivity via solid-state shear mixing. *E-Polymers* 21: 520–532. https://doi.org/10.1515/epoly-2021-0039

41. Seretis GV, Manolakos DE, Provatidis CG (2018) On the graphene nanoplatelets reinforcement of extruded high density polyethylene. *Composites Part B* 145: 81–89. https://doi.org/10.1016/j.compositesb.2018.03.020

42. Yang SY, Lin WN, Huang YL, et al. (2011) Synergetic effects of graphene platelets and carbon nanotubes on the mechanical and thermal properties of epoxy composites. *Carbon* 49: 793–803. http://dx.doi.org/10.1016/j.carbon.2010.10.014

43. Fitaroni LB, Lima JAD, Cruz SA (2015) Thermal stability of polypropylene–montmorillonite clay nanocomposites: Limitation of the thermogravimetric analysis. *Polym Degrad Stab* 111: 102–108. https://doi.org/10.1016/j.polymdegradstab.2014.10.016

44. Chacon JM, Caminero MA, Garcia-Plaza E (2017) Additive manufacturing of PLA structures using fused deposition modelling: Effect of process parameters on mechanical properties and their optimal selection. *Mater Design* 124: 143–157. https://doi.org/10.1016/j.matdes.2017.03.065

45. Shishevan FA, Akbulut H, Mohtadi-Bonab MA (2017) Low velocity impact behavior of basalt fiber-reinforced polymer composites. *J Mater Eng Perform* 26: 2890–2900. http://dx.doi.org/10.1007/s11665-017-2728-1

46. ASTM Int. West Conshohocken (2005) Standard test method for measuring the damage resistance of a fiber-reinforced polymer matrix composite to a drop-weight impact event. Available from: https://www.astm.org/d7136_d7136m-15.html.

47. Niu P, Liu B, Wei X (2011) Study on mechanical properties and thermal stability of polypropylene/hemp fiber composites. *J Reinf Plast Comp* 30: 36–44. http://dx.doi.org/10.1177/0731684410383067

48. Feng J, Safaei B, Qin Z, et al. (2023) Bio-inspired metallic cellular material with extraordinary energy dissipation capability. *Chem Eng J* 475: 146382. http://dx.doi.org/10.1016/j.cej.2023.146382

49. Xie XL, Fung KL, Li RKY, et al. (2002) Structural and mechanical behavior of polypropylene/maleated styrene-(ethylene-co-butylene)-styrene/sisal fiber composites prepared by injection molding. *J Polym Sci B Polym Phys* 40: 1214–1222. https://doi.org/10.1002/polb.10175

50. Hillam L (2004) Alcohol and temperance in modern history: An international encyclopaedia. *Ref Rev* 18: 18–19. https://doi.org/10.1108/09504120410552480

51. Gutmann V (1967) *Halogen Chemistry*, Amsterdam: Elsevier. https://doi.org/10.1016/B978-0-12-395589-0.X5001-9

52. Yang Z, Wang X, Wang J, et al. (2009) Pulsed-plasma polymeric allylamine thin films. *Plasma Processes Polym* 6: 498–505. https://doi.org/10.1002/ppap.200800195

53. Dai J, Liu X, Xiao Y, et al. (2015) High hydrophilicity and excellent adsorption ability of a stretched polypropylene/graphene oxide composite membrane achieved by plasma assisted surface modification. *RSC Adv* 5: 71240–71252. https://doi.org/10.1039/C5RA10310J

54. Yang Z, Wu J, Wang X, et al. (2012) Inspired chemistry for a simple but highly effective immobilization of vascular endothelial growth factor on gallic acid-functionalized plasma polymerized film. *Plasma Processes Polym* 9: 718–725. https://doi.org/10.1002/ppap.201100199

55. Xu T, Li Y, Chen J, et al. (2018) Improving thermal management of electronic apparatus with paraffin (PA)/expanded graphite (EG)/graphene (GN) composite material. *Appl Therm Eng* 140: 13–22. http://dx.doi.org/10.1016/j.applthermaleng.2018.05.060

56. Moradkhani G, Fasihi M, Parpaite T, et al. (2020) Phosphorization of exfoliated graphite for developing flame retardant ethylene vinyl acetate composites. *J Mater Res Technol* 9: 7341–7353. https://doi.org/10.1016/j.jmrt.2020.04.085

57. Hadjiivanov KI, Panayotov DA, Mihaylov MY, et al. (2020) Power of infrared and raman spectroscopies to characterize metal-organic frameworks and investigate their interaction with guest molecules. *Chem Rev* 121: 1286–1424. https://doi.org/10.1021/acs.chemrev.0c00487

58. Fang J, Zhang L, Sutton D, et al. (2012) Needleless melt-electrospinning of polypropylene nanofibres. *J Nanomater* 2012: 382639. https://doi.org/10.1155/2012/382639

59. Zaman HU, Hun PD, Khan RA, et al. (2014) Polypropylene/clay nanocomposites: Effect of compatibilizers on the morphology, mechanical properties and crystallization behaviors. *J Thermoplast Compos Mater* 27: 338–349. https://doi.org/10.1177/0892705712446017

60. Gaska K, Xu X, Gubanski S, et al. (2017) Electrical, mechanical, and thermal properties of LDPE graphene nanoplatelets composites produced by means of melt extrusion process. *Polymers* 9: 11. https://doi.org/10.3390/polym9010011

61. El Achaby M, Arrakhiz F, Vaudreuil S, et al. (2012) Mechanical, thermal, and rheological properties of graphene-based polypropylene nanocomposites prepared by melt mixing. *Polym Compos* 33: 733–744. https://doi.org/10.1002/pc.22198

62. Olowojoba GB, Eslava S, Gutierrez ES, et al. (2016) In situ thermally reduced graphene oxide/epoxy composites: Thermal and mechanical properties. *Appl Nanosci* 6: 1015–1022. https://doi.org/10.1007/s13204-016-0518-y